Novosibirsk State University

As a manuscript

Vijayanand Kuttikattu Vadakeppattu

Optimisation of Time Projection Chamber parameters for Super Charm Tau Detector

1.3.15 – Physics of atomic nuclei and elementary particles, high energy physics

A thesis submitted in fulfillment of the requirements
for the degree of Doctor of Philosophy (Ph.D)
in Physical and Mathematical Science

Research Supervisor:
Andrey Valarevich Sokolov
Candidate of science (Physical and Mathematical Sciences)
Physics Department, Novosibirsk State University.

Novosibirsk – 2024

Declaration

I Vijayanand Kuttikattu Vadakeppattu, hereby declare that the work presented in this thesis titled, in fulfillment of the degree of **Doctor of Philosophy** in **Physical and Mathematical Science** in the Department of Physics, Novosibirsk State University is an authentic record of my work carried out during the period from September 2017 to September 2023 under the guidance of Dr. Andrey Valerevich Sokolov, Senior lecturer, Department of Physics, Novosibirsk State University.

Signature:
Date:

Epigraph

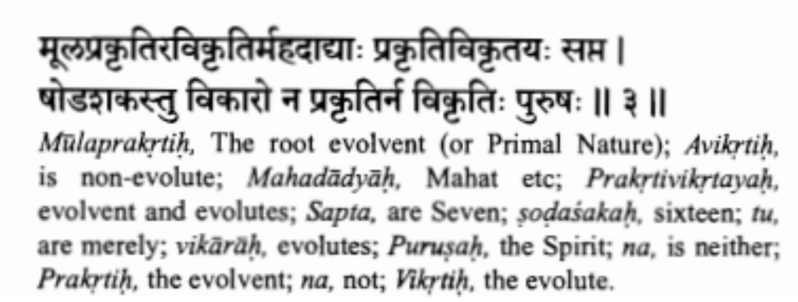

मूलप्रकृतिरविकृतिर्महदाद्याः प्रकृतिविकृतयः सप्त ।
षोडशकस्तु विकारो न प्रकृतिर्न विकृतिः पुरुषः ॥ ३ ॥

Mūlaprakṛtiḥ, The root evolvent (or Primal Nature); *Avikṛtiḥ,* is non-evolute; *Mahadādyāḥ,* Mahat etc; *Prakṛtivikṛtayaḥ,* evolvent and evolutes; *Sapta,* are Seven; *ṣoḍaśakaḥ,* sixteen; *tu,* are merely; *vikārāḥ,* evolutes; *Puruṣaḥ,* the Spirit; *na,* is neither; *Prakṛtiḥ,* the evolvent; *na,* not; *Vikṛtiḥ,* the evolute.

Acknowledgement

I want to express my sincere gratitude to my family, teachers, and friends for their unwavering support throughout my academic journey. Their encouragement has been a constant source of motivation.

I am particularly grateful to my supervisor, Dr. Andrey Sokolov, for his invaluable guidance and mentorship. His expertise and insights have been instrumental in shaping this research project. I would also like to thank my research group members, Timofei Maltsev and Lev Shekhtman, for their collaboration and support. Their contributions have been essential to this work.

Abstract

The Budker Institute of Nuclear Physics is developing a Super Charm-Tau Factory (SCTF) project which consists of a collider with energy 2-5 GeV and luminosity 10^{35} $\mathrm{cm}^{-2}\mathrm{s}^{-1}$. The project aims to study the effect of CP-violation in the decay of charmed particles, test the standard model in the decay of tau lepton, and search and study entirely new forms of matter: glueballs, hybrids, etc. The main features of the Super Charm-Tau Factory are a wide range of energies, high luminosity, and the possibility of conducting experiments with longitudinally polarized electron beams.

The physics program of SCTF requires a universal magnetic detector with a field of about 1.5T. The Super Charm-Tau Detector (SCTD) system is a combination of several detectors. The inner tracker is placed immediately after the vacuum pipe to measure the secondary vertices of the decay of short-lived particles. The inner tracker is followed by the drift chamber, which is the main tracking and momentum-measuring detector. The particle identification system will be placed after the drift chamber and a high-resolution electromagnetic calorimeter is placed to detect the neutral particles. A nine-layered muon detector is placed after the calorimeter to separate muons from hadrons. The main goal of our work are:

- Develop a simulation package in the aurora framework for the Time Projection Chamber (TPC) as the inner tracker.
- Optimize the thickness of TPC to make it possible for soft pions to cross the TPC wall.
- Select a suitable gas mixture for TPC as a drift medium to achieve transverse resolution less than 200 m. The drift velocity of electrons in the medium should be not less than 5 cm/μs. To minimize the complexity of the field cage, the applied electric field is limited to a range of 100 and 1000 V/cm.

- Conduct a simulation study to minimize the Ion Backflow (IBF), which can distort the applied electric field. The proposed electric field for this simulation is 50 kV/cm.
- Build a simulation package to understand the real-time detector response.

The above-mentioned goals have a significant impact on the performance of the TPC thus on the inner tracker.

The main new results obtained during our study are following:

Study of transport properties of electrons in various gas mixtures: Choosing a gas mixture for TPC was one of our main objectives. We did a simulation study with both argon and neon-based gas mixtures to choose a suitable gas mixture as the drift medium of TPC. The study is important as the performance of the TPC depends on the drift. Our study found that argon as a primary gas in the gas mixture as electrons can achieve high drift velocity with reasonable diffusion in the electric field range of 100 to 1000 V/cm.

Study of spatial resolution to finalize gas mixture: Our detailed simulation study using the charge centroid method to find the transverse resolution and total resolution in 200 and 500 V/cm with more than 20 argon based gas mixtures shows that many gas mixtures, especially with CH_4 and CF_4, can provide resolution below 200 μm. However, the size of the readout pad should be less than 1 mm which may increase the budget. Our study found that two gas mixtures, namely argon with 50% CF_4 and argon with 40%CF_4 and 15% CH_4 meet all the requirements of the inner tracker.

Study of ion backflow (IBF): We did a study to calculate the ratio of ions moving back to the drift volume. The study was done with the applied electric field range in the GEM holes of 10kV/cm to 100 kV/cm and we used two types of Gas Electron Multiplier (GEM) stacks. The first one is the standard GEM and the second GEM is a special GEM with a pitch two times larger than that of the standard GEM. In the first simulation, we used a triple GEM made of standard GEMs. In the second case, we replaced the middle GEM with the special GEM and compared the result with that of the first study. The comparison proved that using a triple GEM with two standard GEM stacks and a special GEM stack in the middle will reduce the IBF. Our study found that the triple GEM as a combination of standard and special GEM will help to reduce the IBF hence proposed the same as the readout system.

The results of this work provide a robust foundation for the design and construction of the SCTF TPC. The optimized gas mixture and GEM configuration are expected to deliver exceptional performance in terms of spatial resolution, ion backflow, and overall tracking efficiency. These findings constitute a significant step towards realizing the scientific goals of the SCTF experiment.

Contents

Chapter 1

Introduction to Super Charm-Tau Factory

1.1. Introduction

The Super Charm-Tau Factory (SCTF) project is an electron-positron collider with a range of center of mass energies from 2 to 6 GeV with luminosity 10^{35} $cm^{-2}s^{-1}$. All states of charm including charmed mesons, the bound state of c($\bar{c}$), charmonium mesons, and baryons comprising one c($\bar{c}$) can be produced with this energy range. Moreover, above 3.6 GeV, the τ lepton pairs can be produced [1]. Due to its high luminosity, the SCTF will be a plentiful source of τ leptons and charmed particles. The main goal of the SCTF project is to study the process in which c quark or τ lepton is involved in the final state. The data samples taken from SCTF are expected to be two orders of magnitude higher than that of similar projects such as BESIII. With its high luminosity, it is expected that 10^9 τ leptons, 10^9 D mesons and about 10^{12} J/ψ mesons will be produced in SCTF in a year. Such a huge data sample will allow a well-ordered study of all states of quarks in the first two generations.

Another important physics study that will be done with SCTF is the search for exotic states and the study of their properties According to quantum chromodynamics (QCD), in addition to standard baryons and mesons consisting of three and two quarks, didn't rule out the possibility of the existence of heavy quarkonium (four or five quark states) and the bound state of gluons (the carrier of strong interactions) [2]. Such states are possible as gluons unlike photons, possess strong or color charge. Even though some of the heavy quarkonium states are observed, our understanding of their properties is very poor. QCD predicts both quark-gluon states and states that consist of only gluons, called glueballs. The hybrids and glueballs are the new forms of matter and form only through strong interaction. The physics program of SCTF is explained in detail in the following sections.

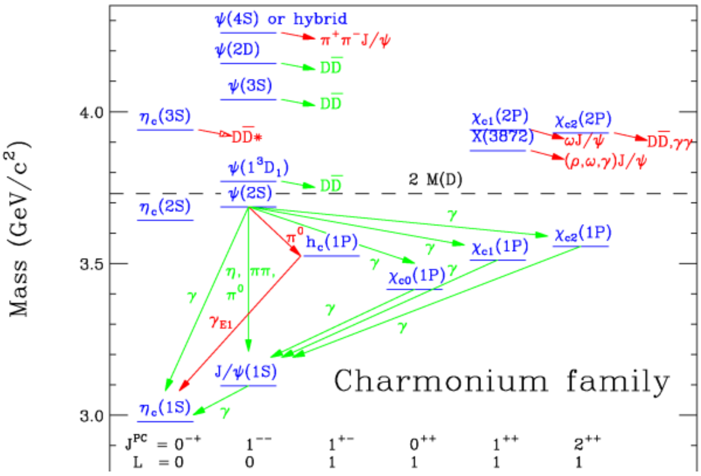

Figure 1.1: Charmonium system and transitions. Red (dark) arrows indicate recently discovered decay and transitions between the levels. The dashed line shows a production threshold for a pair of charmed mesons [1]

.

1.2. Charmonium

The charmonium states are shown in figure 1.1. The charmonium states will decay to hadrons containing u, d, and s quarks as these states are lying below the threshold of D meson production. It is expected that during one experimental season, about 10^{12} J/ψ and 10^{11} ψ(2S) can be produced. About 10^{10} χ_{xj} and η_c mesons can be produced from the decay of J/ψ and ψ(2S) [3]. The rare radiative transition $\psi(2S) \rightarrow \eta_c(2S)\gamma$ with branching fraction $7 \pm 5 \times 10^{-4}$ [3] will be helpful to observe η_c. The data samples will be helpful to understand the properties of $c\bar{c}$ in detail.

A systematic study of low-lying charmonium states is an important task of SCTF. The knowledge about the decay of low-lying states is very less and only 45% of the hadronic transition for the best-studied J/ψ meson has been measured so far. At SCTF, the precision measurement of hadronic transition between low-lying charmonium states with emission of one or two π meson, η meson, $h_c \rightarrow 3\gamma$ decay, etc. can be done. Another physics study that will be done in SCTF is the phenomena that cannot describe by the standard model such as violation of lepton flavor conservation and violation of CP parity. These studies can be done using a large number of samples of ψ meson decay. One can observe the violation of conservation of lepton flavor from the decay $J/\psi \rightarrow ll'$, where

l, l' are e and μ, and τ. The branching fraction of such decays can be related to that of τ, μ decays to three leptons through an independent way [4] [5]. It is possible to obtain branching fractions (J/$\psi \rightarrow \mu$e) $< 2\times\ 10^{-13}$ and (J/$\psi \rightarrow \tau l$) $< 6\times\ 10^{-9}$ from ($\mu \rightarrow ee^+e^-$)$< 10^{12}$[3] and ($\tau \rightarrow \mu e^+e^-$) $< 2.7 \times 10^{-8}$ [5]. By keeping a limit on $\tau \rightarrow \mu e^+e^-$ decay with data sample 5×10^8 τ lepton pairs, J/ψ decays can be more sensitive to lepton flavor violation than that of τ lepton.

Another physical property beyond the standard model that can study at SCTF is the non-zero electric dipole moment of quarks and leptons, which will lead to the violation of CP parity and lepton number conservation. One can observe the CP violation using three-body decays of J/ψ mesons such as J/$\psi \rightarrow \gamma\phi\phi$. With this decay and 10^{12} J/ψ mesons, it is possible to obtain a sensitivity of $10^{-15}e{\cdot}$cm level for c-quarks [6]. Other than above mentioned three-body decay, the two-body decay J/$\psi \rightarrow \Lambda\bar{\Lambda}$ can be used for the search of CP violation. A limit of level $5 \times 10^{-19}e{\cdot}$cm [7] on the Λ hyperon electric dipole moment can be set by using this decay. Such a limit is two orders of magnitude more strict than the existing limit.

An important study about charmonium state that can be done at SCTF is the weak J/ψ decay. The semi leptonic and hadronic decays (J/$\psi \rightarrow$ D$_s^*l\mu$, D$_sl\mu$ and J/$\psi \rightarrow$ D$_s^+\rho^-$, D$_s^{*+}\pi^-$) of J/ψ mesons can be measured at SCTF. These decays have branching fractions $3-4\times10^{-9}$ [8, 9]. In addition, the weak process violating the C parity, for e.g, J/$\psi \rightarrow \phi\phi$ with expected branching fraction $\approx 10^{-8}$ can be observed at SCTF. In the last decade, many charmonium states with mass above the open charm threshold have been observed in the experiments such as LHCb, BESIII, BABAR, etc [10]. However, only a few of them are identified as excited $c\bar{c}$. Many of these states have non-zero electric charges which indicate their exotic nature. The theory which tries to explain the properties of new states declared the existence of four quark states[11]. With statistics 10-100 times higher than that accumulated by BESIII, SCTF will give a good opportunity to study these exotic charmonium-like states.

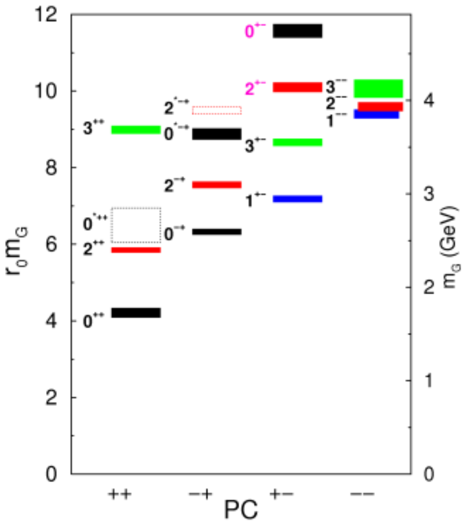

Figure 1.2: the spectrum of glueballs

1.3. Spectroscopy of light quarks

The light charmonium states which have a mass less than two times the mass of D mesons can decay to hadrons consisting of light quarks (u,d,s). At SCTF, one can study selected decay modes of $c\bar{c}$ with practically any quantum numbers and this will make SCTF a sole laboratory for the study of properties of light mesons composed of u, d, s quarks. Another important task of SCTF in the search for hybrid states ($q\bar{q}g$) and glueballs (bound state of two gluons). According to lattice QCD, the light glueballs (J^{PC} = 0^{++}, 2^{++}, 0^{+-}) have mass less than 3 GeV [12]. The spectrum of glueball obtained from [12] is given in fig 1.2. At SCTF, with a large number of J/ψ meson production, one can study the properties of glueballs using the decay J/$\psi \to \gamma gg$ which is followed by the hadronization of the gluons. The probability of this decay is about 9%. The advantage of the study glueball production is such a study should be complemented by the production of two-photon mesons. To measure the glueball fraction from the decay, one should study the properties of mesons in different processes and their decay modes in detail. For example, for scalar mesons (f_0, a_0, K_0^*), the gluon component will appear as an unusual ratio of decay probabilities for two quark mesons and appear as an extra f_0 meson which cannot fit in the two quark states. At present state, there are only two candidates for hybrid light quarks: $\pi_1(1400)$ and $\pi_1(1600)$. However, the existence of these states is not confirmed yet. At SCTF, these states can be observed through the S-wave decay $\chi_{c1} \to \pi\pi_1$ and P-wave decay $J/\psi \to \rho\pi_1$. The lightest hybrid with quantum number 0^{-+} is expected to have a mass region around 2 GeV and this state can be searched either $\chi_{c0} \to \pi\pi_1$ decay or the decays of ψ mesons.

1.4. D mesons

The charged $D^{\pm}$ of quark structure (cd), $D_s^{\pm}$ with structure (cs) and neutral D^0 and $\bar{D}^0$ with structure (cu) are the three main types of charmed mesons. In SCTF, with its high luminosity, about 10^9 pairs of D mesons and 2×10^7 pairs of D_s mesons can produce in one experimental season. Even though these numbers do not exceed the number of D mesons produced in B factories, where the e^+e^- c.m energy is 10.58 GeV, The production of D mesons in SCTF at 3.7 GeV will allow the measurement at low energy and more precise result with lower statistics. The orbital excited states of D meson can be described using heavy quark effective theory. Fig 1.3 from [1] showing the classification scheme of low-lying levels of D meson. Here the states are classified by the total angular momentum of the light quark $\vec{j}_q$ and spin of the meson $\vec{J} = \vec{j}_q + \vec{s}_Q$. The low-lying levels of D meson have six states. The ground state has two states $J^p_{j_q} = 0^-_{1/2}$ and the vector state with the $J^p_{j_q} = 1^-_{1/2}$ which is called D^* meson. The D^{**} mesons are states with L = 1 with two doublets with $j_q = 1/2$ and $j_q = 3/2$ which is applicable to all types of D mesons. Another state of D mesons is the D^{**} states with L = 1. This state has two doublets with $j_q = 1/2$ ($J^P_{j_q} = 0^+_{1/2}, 1^+_{1/2}$) and $j_q = 3/2$ ($J^P_{j_q} = 1^+_{3/2}, 2^+_{3/2}$). The decay of D^{**} to the $D\pi$ system is constrained by the angular momentum and conservation of parity. The state with $j_q = 1/2$ has a decay width of hundreds of MeV and is hence expected to be broad while the $j_q = 3/2$ is expected to be narrow as it has a small decay width of tens of MeV. The spectrum of neutral D mesons from the relativistic quark model [13] is given in figure 1.4 and this shows good agreement with measured values of ground and orbital excited states. However, the experimental information about the D_j and D_{sj} mesons are incomplete and their properties require further theoretical and experimental studies. The precise knowledge about these states is crucial for the determination of Cabbibo-Kobayashi-Maskawa (CKM) matrix elements, understanding semileptonic b $\to$

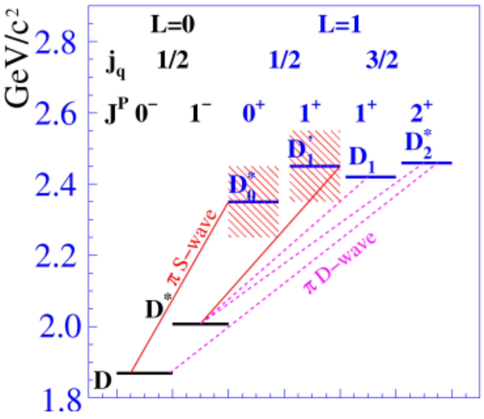

Figure 1.3: D meson levels

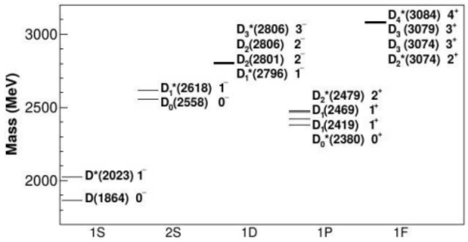

Figure 1.4: The mass spectrum for neutral D mesons in the relativistic quark model.

c decays, and searching for the evidence for "new physics". In SCTF it will be possible to produce and study the properties of D$_j$ and D$_{sj}$ states through various reactions and a detailed measurement of cross sections of exclusive charm productions will help for the discovery of new states in this family.

The detailed study of the decay of charmed mesons is another important physics program of SCTF. The SCTF allows a detailed study of the decays of D and D$_s$ mesons which includes measurement of decay probability with high precision and Dalitz plot analyses for three-body decays and the analysis of four-body decay distributions. The decay constants and form factors can be calculated accurately in the lattice QCD (LQCD) framework. The precision measurements of D decays will control these calculations and will help to reduce the uncertainties in the extraction of CKM matrix elements from various B meson decays. To measure the angles of a unitary triangle ($\beta(\phi_1)$ and $\gamma(\phi_3)$) at a super B-factory, precise measurements of neutral D-meson data such as amplitude ratio of D$_0$ and $\bar{D}^0$ decay into K$^+$ π^- and the strong phase difference between these amplitudes, D$_0$ and $\bar{D}^0$ mixing parameters and Dalitz distributions for the three-body hadronic decays. All these data can be obtained at SCTF. The width of a leptonic D^+ decay in SM is given by

$$\Gamma(D^+ \to l^+\nu) = \frac{G_F^2}{8\pi} f_D^2 m_l^2 M_D (1 - \frac{m_l^2}{M_D^2})^2 |V_{cd}|^2$$

where m_l and M_D are masses of lepton and D-meson, G_F is Fermi constant. The experimental data obtained from [14, 15, 16] from the leptonic decay of D and D_s shows that the values obtained for the decays constants of D and D_s are consistent with the most accurate prediction made by LQCD calculations. Checking of lepton universality is another test required in SM. The current experimental values obtained for this are not accurate and more accurate experimental data is required to confirm the predictions of Standard Model (SM). Even though the semi-leptonic D decays into pseudoscalar π and K meson are studied extensively, the other semi-leptonic D and D_s modes are measured with poor accuracy, and large statistics are needed for measurement with good accuracy which can be collected at SCTF.

The study of $D^0\bar{D}^0$ mixing is another important physics goal of SCTF. The eigenstate of the mass matrix due to the $D^0 \Leftrightarrow \bar{D}^0$ transition are

$$|D_1\rangle = \frac{1}{\sqrt{|p^2| + |q^2|}}(p|D^0\rangle + q|\bar{D^0}\rangle)$$

$$|D_2\rangle = \frac{1}{\sqrt{|p^2| + |q^2|}}(p|D^0\rangle - q|\bar{D^0}\rangle)$$

These transitions are due to the interactions which change the charm quantum number by 2. For a CP variant interaction, p = q and eigenstate $|D_1\rangle$ and $|D_2\rangle$ have definite internal parity. At SCTF, the production of $D^0\bar{D}^0$ in a coherent state with different C parities will allow the measurement of mixing phenomena. However, in symmetric SCTF (where colliding electrons and positrons have the same energy), due to the short lifetime of D-mesons, the study of the time evolution of $D^0\bar{D}^0$ will not be possible and hence, the analysis will focus on the time-integrated values. Analyzing the decays to some specific final states, suggested by [17]. Another interesting experiment that can be done at SCTF is the search for CP violation in $D_{(s)}$ decays. According to the standard model, the CP asymmetry is very small in the reactions with charmed particles [18]. There are three different types of CP violations:

- In $\Delta C = 1$ transitions, CP violation can observe as the inconsistency in the amplitude of $D_{(s)}$ meson decay A_f and corresponding CP conjugate amplitude $\bar{A}_{\bar{f}}$.
- The CP violation will reveal in the $D^0\bar{D}^0$ mixing due to $\Delta C = 2$ transitions as deviation from the unity in the ratio $\mathrm{R}_m = |p/q|$.
- The CP violation can be observed in the neutral D-meson decay with mixing ($D^0 \rightarrow \bar{D}^0 \rightarrow f$) and without mixing ($\mathrm{D}^0 \rightarrow f$)

The CP violation in the mixing can be observed as a discrepancy in semi-leptonic decays when the sign of decay lepton is incorrect i.e the $\Gamma(D^0 \rightarrow l^+X) \neq \Gamma(D^0 \rightarrow l^-X)$. Also, CP violation can be observed as a difference between decay widths for charged D mesons.

$$A_{\pm}^{CP} = \frac{\Gamma(D^- \rightarrow f^-) - \Gamma(D^+ \rightarrow f^+)}{\Gamma(D^- \rightarrow f^-) + \Gamma(D^+ \rightarrow f^+)}$$

However, for the neutral D mesons, the asymmetry parameter encompasses contributions from all three types of CP violation. In the measurement of CP asymmetries, the systematic error is dominated by uncertainties in particle identification and track reconstruction, and at SCTF, these errors can reduce to 10^{-3}- 10^{-4}. The error in charge asymmetry measurements can be decreased by minimizing the thickness of the material before and inside the tracking system of the SCTF detector.

1.5. Physics of τ leptons

Another important physics program of SCTF is the study of τ-leptons. In SCTF, τ-leptons are produced in the reaction $e^+e^- \rightarrow \tau^+\tau^-$. About 2.1 $\times 10^{10}$ pairs are expected to produce during the operation of SCTF. A dedicated run near $e^+e^- \rightarrow \tau^+\tau^-$ threshold will make high precision measurements of branching fractions and spectral functions of possible hadronic τ decays. These measurements can be used to determine strong coupling constant α_s, the mass of s-quark m_s, and CKM matrix element V_{us}. The decays $\tau^+ \rightarrow \pi^+\nu$ and $\tau^+ \rightarrow K^+\nu$ as well as measurement of branching fractions with high precision will help to improve lepton universality tests in the interaction of W-bosons with lepton current. A study on lepton flavor violation (LFV) is also possible in SCTF. LFV decays such as $\tau \rightarrow \mu\gamma, \tau \rightarrow lll' or \tau \rightarrow lh$ where l, l' are muons or electrons and h is hadron are sensitive to new physics. Beyond standard models predicts branching fraction about $10^{-7} - 10^{-10}$ for these decays. In spite of fewer statistics in comparison with other experiments such as KEKB, SCTF will have better sensitivity (below 10^{-9}) for such decays. Another important physics study in SCTF is CP violation (CPV) in the lepton sector. This is important to understand the baryon asymmetry of the universe which cannot be explained using CPV in the quark sector alone.

Other than the above-discussed programs, the physics program of SCTF will be useful to study rare decays of D and D_s offering one of the efficient ways to explore beyond the standard model (BSM). Three different types of charmed meson decay, flavor-changing neutral current (FCNC) decays via the weak neutral current, lepton-flavor-violating (LFV) decays, and lepton number violating decays. Also, a detailed study about charmed meson can also perform at SCTF. Charmed baryon can produce at SCTF through the reaction $e^+e^- \to B_c\bar{B}_c$. Even though many charmed mesons are produced at B-factories and BES III, information about their properties is poor. At SCTF, with a luminosity of $200\,\mathrm{fb}^{-1}$, 10^8 $\Lambda_c\bar{\Lambda}_c$ can be produced. This will allow one to conduct a detailed study of the properties of Λ_c using the double tag method. Production of the large number of $\Lambda_c\bar{\Lambda}_c$ pairs will help in the search for CP violation in the decay of Λ_c. In SCTF longitudinally polarized initial beams can provide the possibility to study effects such as CPV, and Michel parameters. Other than the physics programs explained above, SCTF also aims to conduct a study about two-photon physics, spectroscopy of light quarks, and measurement of a cross-section of e^+e^- annihilation into hadrons below 5 GeV.

Chapter 2

The Super Charm-Tau Detector

2.1. Detector Overview

The physics program of SCTF explained in the previous section cause some outstanding challenges on a detector. Moreover, such a program required a universal magnetic detector of the field about 1T and should be capable of detecting charged and neutral particles with 4π solid angle coverage and spatial resolution. The requirements of Super Charm-Tau Detector (SCTD) are given below [1].

- The detector should have high momentum and energy resolution for charged particles and photons. Also, the particle identification system should have the best parameters among the existing and under-construction detectors. The detector trigger should be powerful enough to select physics events and suppress a very high background rate.

- To select rare D decays, K/π separation greater than 3σ needed. In addition, μ/π separation up to 1.2 GeV/c momentum is required for suppression of π meson background and for the selection of $\tau \rightarrow \mu\gamma$.

- To achieve high data-taking efficiency, the data acquisition system should be able to read events at a rate of 300-400 kHz with an event length of about 30 kB.

The subsystems of the Super Charm-Tau Detector are a vacuum chamber, inner tracker, drift chamber, particle identification system, electromagnetic calorimeter, superconducting coil, and an iron yoke with a muon system inside. An overview of all subsystems is given below.

2.2. Vacuum Chamber

Beam collisions took place inside the vacuum chamber which has a length of 600 mm and a radius of 20 mm with a thickness of 1mm. The inner wall of the vacuum chamber

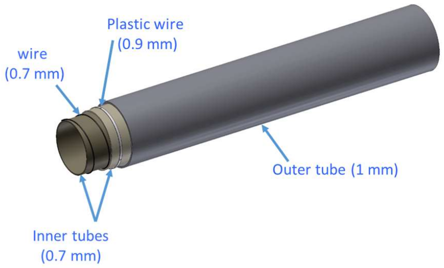

Figure 2.1: Multi-layer vacuum pipe

is coated with a 0.05 mm copper layer to suppress the background from the synchrotron radiation. Figure 2.1 shows the simulated geometry of a multi-layer vacuum pipe. The primary estimation for the SCTF vacuum chamber shows 100 W/m thermal load due to high order modes (HOMs) and image current. The main task is to construct and test a prototype for the multi-layer vacuum chamber inside the cryostat to provide tolerable heating of the Forward Field (FF) magnet.

2.3. Inner Tracker

Inner Tracker (IT) is placed between the vacuum chamber and the drift chamber. The main task of IT is to detect secondary vertices from decays of short-lived particles like Λ or K_s^0 as well as increase the lever arm of the drift chamber for better momentum resolution. As it is placed near the beam pipe, IT should handle high particle flux when the collider operates at maximum luminosity. The inner tracker provides detection solid angle up to 98%. The IT is located in a cylindrical volume of 600 mm in length, with the inner diameter and an outer diameters of 50 mm and 400 mm, respectively. The data of IT can process either with the drift chamber to get better momentum resolution or alone to reconstruct secondary vertices. Detailed descriptions of different options for IT are given in the next chapter.

2.4. Drift Chamber

Drift Chamber (DC) is one of the important subsystems of SCTD for tracking and measuring momentum. The Cylindrical DC of SCTD has a 2m length with inner and

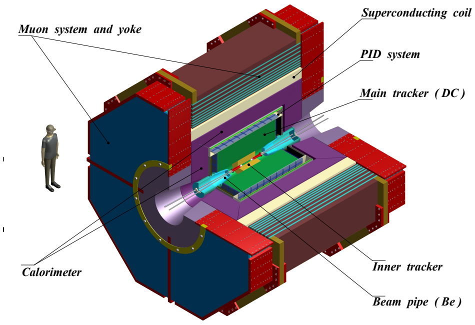

Figure 2.2: Detector for the Super Charm-Tau factory in Novosibirsk.

outer diameters of 0.4 and 1.6 meters respectively. Endplates are made of 24 mm thick Aluminum and can carry an axial load of about 32000 N [1]. The maximum deflection of the endplate after loading is about 28% of 7 mm wire elongation under tension. The inner cylinders in DC are made of 1.5 mm Carbon fiber and 5 mm thick fiberglass. While the inner cylinder carries 40% of the wire load, the rest is carried by the outer cylinder. As RF shield for the chamber, Aluminum foil of 28 μm thick on the inner surface and 100 μm on the outer surface is used. The outer shell is competent to withstand temperature variation of ± 20^0C and pressure 30 mbar. For particles at normal incidence, the total thickness of DC is 1.08% X_0 in which 0.2% X_0 contribution from wires and about 0.25% X_0 from the gas mixture. DC has about 40 layers with 7100 close-packed hexagonal cells. Each cell has a radius of about 1 cm and has a single sense wire surrounded by field wires.

The layers in DC are grouped into super layers with the same wire orientation and an equal number of cells in each layer. There are four such super layers each containing ten layers. The super layer can make as axial (parallel to the z-axis) and small-angle stereo (with changing 7-12 cells in endpoint wire in alternate directions). Stereo angles are chosen in such a way that the drilling patterns are identical for two end plates. It can vary between ±32 mrad and ±52 mrad. Drift cells are hexagonal in shape with 11.9 mm in radial and 19 mm in azimuthal directions. The advantage of the hexagonal shape is its approximate circular symmetry over the large portion of the cell. The sense wires have a diameter of 20 μm and are made of tungsten-rhenium. Sense wires are tensioned by a weight of 30 g and have a deflection of 200 μm in the middle length due to gravity. The tension of field wires is 155 g. This is to match the gravitational sag of sense wires within 20 μm. To improve the electrostatic performance and match the gain of boundary cells to the cells of the inner layer, two guard wires are added for the inner or outer boundary of super layers. Hence, a total of three different types of feed-throughs required to accommodate these fields, sense, and clearing wires.

2.5. PID system

The rich physics program of SCTF demands an excellent particle identification system (PID) specifically for the study of rare phenomena beyond SM. PID system for SCTD should fulfill the following requirements;

- perfect μ/π and π/K separation with more than three standard deviation (σ) in the momentum range 0.3-1.2 GeV/c and 0.6-2.5 GeV/c respectively.
- To maintain event rate up to 300 kHz.
- Withstand annual neutron equivalent dose of 2×10^9 $n_e q/\mathrm{cm}^2$ for barrel part and 10^{10} $n_e q/\mathrm{cm}^2$ for endcap part [19].

At present, there are three options for the PID system. These are described below.

2.5.1. FARICH system

Focusing Aerogel Ring Imaging Cherenkov Detector (FARICH) is capable to meet all these requirements. FARICH technique was demonstrated with both simulation and prototype beam test in CERN in 2012 [20, 21]. In the FARICH technique, several aerogel layers with different refractive indices are arranged in such a way that Cherenkov rings from different layers overlap in the photon detector plane. The sketch of the FARICH system for SCTD is shown in fig 2.3. The proposed FARICH system has the following parameters [22].

- The system has two endcaps and barrel parts and cover nearly 4π solid angle.
- The total surface area of the 4-layer aerogel Cherenkov radiator with n_{max}=1.07 and thickness of 35 mm is 17 m^2.

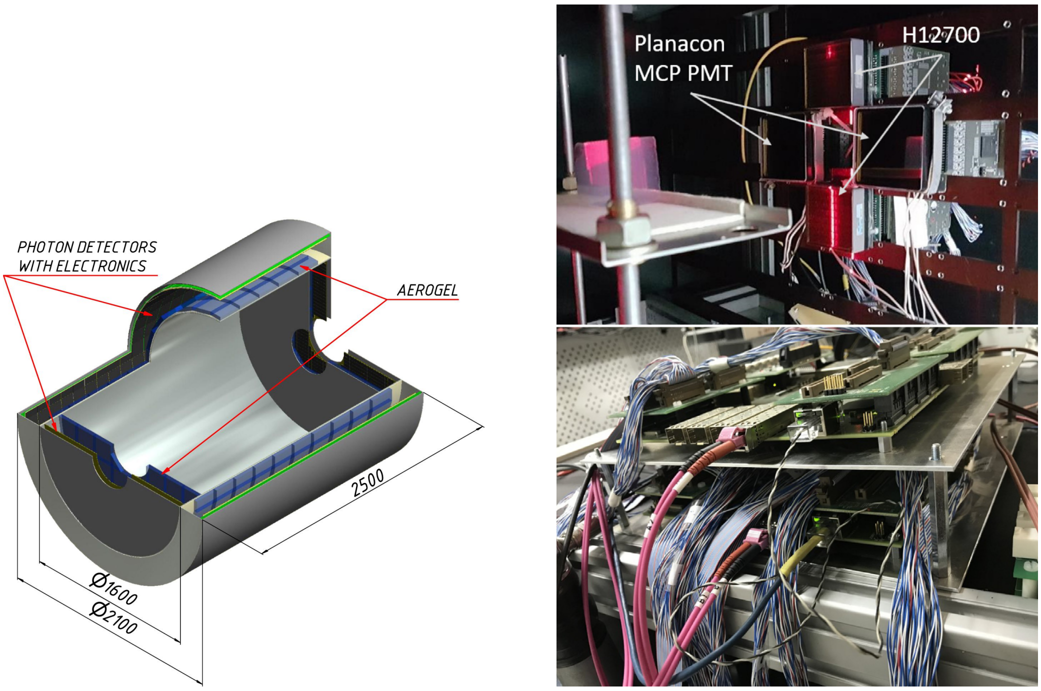

Figure 2.3: a) FARICH-based PID system for the Super Charm-Tau Detector. b) MaPMTs, MCP-PMTs (top), and TRB3 boards (bottom) in FARICH prototype

- The distance between the inner surface of the radiator and the photon detector is 20 cm.
- The total area of position-sensitive photon detectors with pixel size of $3\times\ 3\,\mathrm{mm}^2$ is 21 m^2.
- About 1.6×10^6 readout electronic channels.
- The material budget is within the range of $0.15\,X_0$ and $0.30\,X_0$ depending on the photon detectors technology.

There are two different methods to make a multi-layer stack of several aerogel blocks or a monolithic multi-layer block. The former technique is used in the Belle-II ARICH system [23]. The second option is suggested for SCTD [24]. The first monolithic four-layer aerogel for FARICH was produced in Novosibirsk in 2004 [25]. The beam test for the FARICH prototype with MaPMT readout was carried out in BINP in 2018. The beam test results show a good agreement between experimental and calculated results on the radius resolution with minimum errors. The comparison between experimental

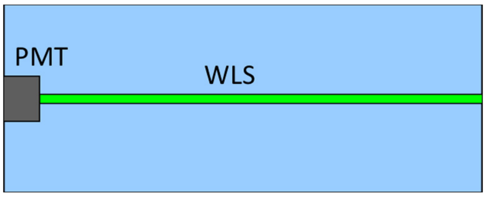

Figure 2.4: Schematic picture of ASHIPH counter

and calculated results helps to calculate track reconstruction uncertainty and multiple scattering [19].

2.5.2. ASHIPH system

The second option for PID is aerogel shifter photomultiplier (ASHIPH) counters. The light collection in the ASHIPH counter is performed by using wavelength shifters (WLS). ASHIPH system is successfully implemented in KEDR detector in VEPP-4M e^+e^- collider at BINP [26]. Figure 2.4 shows the schematic picture of the ASHIPH counter. The proposed ASHIPH system has the following parameters [22].

- Three layer system: one layer with aerogels of refractive index n=1.03 (2000 liters) for π/K separation from 0.6 to 2.0 GeV/c and μ/π separation from 0.4 to 0.6 GeV/c and two layers with aerogels of refractive index n=1.015 (4000 liters) to extend μ/π separation up to 0.8 GeV/c.
- Counter dimensions $18 \times 30 \times 8\,\text{cm}^3$.
- WLS dimension $0.3 \times 28 \times 6\,\text{cm}^3$.
- Silicon photomultipliers (SiPMs) area per counter is $180\,\text{mm}^2$.
- Number of counters in the system is 1400 and the number of SiPMs in the system is 28000.
- Material budget $0.14X_0$.
- System for SiPMs cooling to -40^0C.

2.5.3. ToF+ToP system

Another option for the PID system is a combination of the time of flight (ToF) detector with the time of propagation (ToP) approach providing a time resolution better than 30 ps. The above-mentioned aerogel-based approach cannot provide μ/π separation below 0.3 GeV/c (FARICH) and 0.4 GeV/c (ASHIPH). However, μ/π separation below 0.3 GeV/c is important for semi-leptonic D-meson decays. In SCT Factory, half of the muons produced in such a process have momentum below 0.4 GeV/c. To overcome this problem, the ToF+ToP system is proposed as an extension of μ/π separation capability for one of the above-proposed systems. The proposed ToF system for the SCT detector has 10000 quartz bars ($5 \times 5 \times 250\,\mathrm{mm}^2$) and 1648 multi-anode MCP-PMTs with rectangular shape 40×20 mm. The estimated material budget is $0.14X_0$ [22].

2.6. Electromagnetic Calorimeter

Another important subsystem of SCTF is the electromagnetic calorimeter (EM calorimeter). The main task of SCTF is to search for lepton flavor violation decay $\tau \rightarrow \mu\gamma$ which has to provide a narrow peak in the $\mu\gamma$ invariant mass spectrum. This peak is provided by the energy and spatial resolution of the calorimeter. Also, the decay mentioned above strongly depends on the width of the peak. So, the SCTF needs an EM calorimeter with good energy and coordinate resolution. Following are the tasks of the SCTF EM calorimeter.

- Determination of photon energy and coordinates with maximum accuracy.
- Electron/hadron separation
- K_L detection
- Intensity measurement both online and offline
- generates a proper trigger signal.

Electromagnetic calorimeter based on pure CsI crystals with avalanche photodiodes (APD) and wavelength shifting (WLS) plates are chosen for SCTF. The radiation hardness of CsI crystals with the size and shape of real counters are studied [27, 28]. The pure

CsI crystals were produced using a semiautomatic growth method which provides the high light output and fast-to-total ratio (R_{FT}). The crystals were exposed to Bremsstrahlung γ-rays produced in the Pb converter by electrons of energy 1.4 MeV and current up to 70 mA from industrial accelerator ELV-6. The dose accumulated was measured using a sensor assembled from small Cs(Tl) crystal and a silicon PIN photodiode for light output. Current from the photodiode is proportional to the light intensity from the crystal or the dose rate. Measurement of scintillation characteristics was studied by placing the crystal vertically in front of UV sensitive photomultiplier tube (PMT) without any optical contact and irradiated by 662 keV photons from collimated ^{137}Cs radioactive source which could be moved along the crystal axis. The PMT signal was digitized with a charge-sensitive amplitude to a digital converter (CDC) after amplification. The light output of the studied crystals was normalized using light output from a small reference crystal made of pure CsI wrapped in Teflon. The radiation hardness of 14 crystals was studied with radiation doses up to 14.3 krad. Most of the crystals showed less than a 20% decrease in light output for a 14.3 krad dose of irradiation. Some of these crystals have satisfactory light output and R_{FT}. This work provides a strong correlation between radiation hardness and scintillation characteristics. Simulation of calorimeter design and calculation of coordinate and energy correction functions are studied [29]. The standard counter with CsI (pure) crystals, wavelength shifting plate (WLS) coated with nanostructured organosilicon luminophores (NOL-9), avalanche photodiodes (APD) coupled to charge sensitive pre-amplifiers developed and tested in Budker Institute of Nuclear Physics [30]. The prototype will be studied on a test beam facility in BINP in the near future.

2.7. Muon system

The Muon system in SCTD has nine layers of coordinate detectors in the barrel and eight layers in the endcap[1]. Barrel and endcap cover $64\% \times 4\pi$ and $30\% \times 4\pi$ respectively. The Muon system separates muons from the large number of hadrons produced in e^+e^- annihilation. The range of muons is determined by the loss of ionization energy in the medium and that of hadrons by finding their energy loss through nuclear interaction with atoms of the absorber. As muon has large kinetic energy than pions and kaons of the same

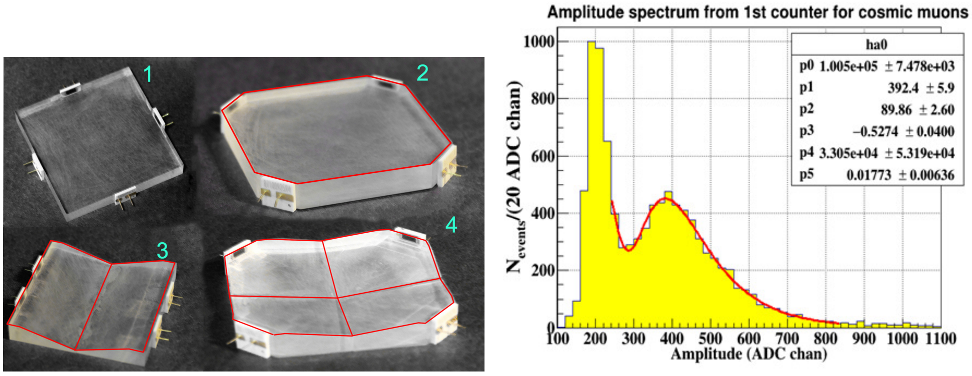

Figure 2.5: (a)PMMA plates of different shapes (b)amplitude spectrum from cosmic particles for the reference counter

momentum, it could lose less energy on the ionization process and leaves a long track in the detector. The detection threshold of the muon system is at particle momentum 0.4-0.5 GeV/c. This is because of the bending of particle tracks in the magnetic field. However, it is difficult to get a good μ/π separation at momentum below 0.8 GeV/c because of fluctuations or pion decay to muon and neutrino in the direction of the initial pion. Information from the FARICH system will be used for the calibration of the muon system.

Chapter 3

A GEM-based TPC

3.1. Introduction

Introduced by D. R. Nygren in 1974 [31], the time projection chamber is a large drift volume with a homogeneous electric field between the drift cathode and the readout system which act as the anode of the drift volume. A field cage is used around the TPC to ensure optimal uniformity of the drift field. Equally spaced conducting strips, such as those etched onto a copper or aluminum coating of a Kapton foil, are positioned between the cathode and anode. These strips are connected through a series of resistors, forming a voltage divider chain that assigns a specific potential to each strip. This arrangement aligns the strips with equipotential surfaces, establishing a homogeneous field throughout the system.

The charged particle traversing through the drift volume of the TPC will ionize the atoms of the gas mixture filled in the drift volume. The free electrons formed due to this ionization process will move toward the anode and the heavy ions will move towards the cathode. A two-dimensional segmented pad plane will be used to get the projection of the track and the third spatial coordinate can be calculated by measuring the time taken by the electrons to reach the readout plane. As the drift velocity of the electrons is constant due to the homogeneity of the electric field, the z-coordinate can be calculated using the time difference between the moment of the particle passage and the time of the signal detection, so $\mathrm{z} = (\mathrm{t} - \mathrm{t}_0)v_d$. The signal has to be amplified before it reaches the pads and this will be done using gas amplification. The following section will discuss the primary ionization, drift, and gas amplification in detail.

3.2. Ionization

When an energetic particle passes through the drift volume of a TPC, it will collide with the gas molecules present in the volume resulting in ionization and excitation. This will create a large number of electron-ion pairs along the path of the particle. The free electrons created in the ionization will drift towards the anode and the heavy ions will move towards the cathode. The electrons will be amplified and collected by the readout system. The X and Y coordinates can be measured from the projection onto the two-dimensional pad plane and the time gap between the transition of the particle and the signal generation will help to measure the Z coordinate, which is perpendicular to the pad plane. This measurement will allow the reconstruction of the particle track in three dimensions. The energy loss dE/dx along the particle track due to ionization can be calculated using the Bethe-Bloch formula

$$-\frac{dE}{dx} = 4\pi N_A r_e^2 m_e c^2 \rho \frac{Z}{A} z^2 \frac{1}{\beta^2} \left[\frac{1}{2} ln(\frac{2m_e c^2 \gamma^2 \beta^2 T_{max}}{I^2}) - \beta^2 - \frac{\delta(\beta\gamma)}{2} \right],$$

where, N_A is Avogadro's constant, r_e is classical electron radius, m_e is the mass of the electron, Z,A are the atomic number, and atomic mass of the absorber material, respectively, ρ absorber density, z is the charge of the traveling particle (in the unit of e), T_{max} is the maximum kinetic energy transferred to the free electron in one collision, δ is the density effect correction of highly relativistic particle and I is the mean excitation energy of the absorber atom. For low energies, the energy loss dE/dx will be inversely proportional to the β^2, and the $\beta\gamma$ will reach ≈ 4. The particles within this energy range are referred to as minimum ionizing particles. For higher energies, the energy deposition increases as a consequence of a logarithmic factor $\ln(\gamma^2\beta^2)$. The energy loss for different particles in Argon with 20% CH_4 in a study given in [32] is shown in fig 3.1. Knowing the particle momentum, and measuring energy loss, this distribution allows the particle identification within an energy limit.

The Bethe-Bloch formula cannot apply to a short absorber distance as it provides only mean energy loss per unit length. The energy deposition follows the Landau distribution for short distances [33] and this distribution is asymmetric with a tail towards higher energies. As the distribution is asymmetric, the energy transferred to the absorber electron in a single collision will vary after each collision. Hence the energy deposition will not be continuous. According to the central limit theorem, the distribution becomes more and more Gaussian-shaped for longer absorber distances and averaging over multi-

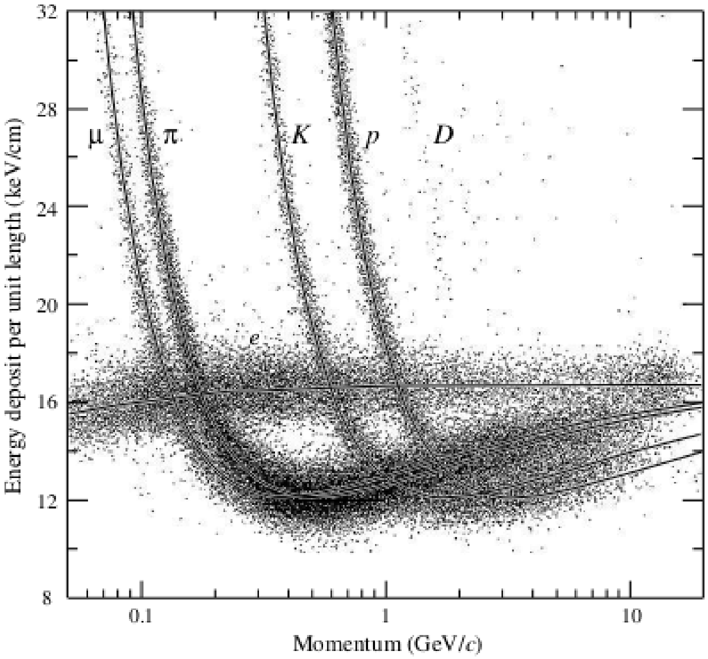

Figure 3.1: Energy loss of highly energetic particles in Argon with 20% CH_4 measured with PEP-4/9 TPC at pressure 8.5 atm

ple measurements.

3.3. Transport Properties in Gases

When the uniform electric field is applied to the drift volume of the TPC, the ions and electrons formed from the ionization process will start to move in opposite directions according to their charge. This movement will separate the electrons from the ions and will prevent the recombination. The ions will move toward the cathode and the electrons will move toward the anode where the electrons will be collected by the readout after amplification.

In a cylindrical detector like TPC, electrons will travel a long distance (from 10s of centimeters to meters depending on the size of the detector) before detection and, in such cases, the drift velocity of the electron and the properties such as diffusion will affect the accuracy of the resolution. This section will discuss drift and diffusion.

3.3.1. Drift of Electrons

The electrons will accelerate in an external electric field E and this will exist until their next collision with the gas molecule. As a result of the collision, the electron will scatter and will lose energy. By averaging over multiple collisions, one can see that the energy lost by the collisions will be equal to the energy gained in the acceleration. This will lead to a motion with mean drift velocity.

$$v^{-}_{drift} = \frac{e}{m_e}\tau E$$

Here, e and m_e are the charge and mass of electron respectively, τ is the mean time between two collisions and will be determined from the cross-section σ and energy loss per collision.

For a specific particle energy ϵ, collision cross-section has a minimum value. For example, in Argon, this value is at $\epsilon = 0.25$ eV. This phenomenon is called the Ramsauer effect [34]. The Ramsauer effect appears when the wavelength of the electron is in the range of the radius of the molecule [35]. The minimum cross-section, maximum τ, will result in maximum drift velocity. The energy loss in collisions depends on the excitation threshold of the gas molecules. For Argon, this value is 11.5 eV however, for quencher gases (the gas added to the cold gas for stable gas amplification), this will be much less, 0.03 eV for methane for instance. So the drift velocity heavily depends on the gas mixture used [36]. Generally, the gas mixture in which electrons have maximum drift velocity in a chosen electric field will be used in TPC.

3.3.2. Drift of Ions

The ions due to their large mass compared to electrons, will move slowly through the drift volume. In a TPC with the standard electric field, the energy gained between two collisions will be equal to or less than the order of the thermal energy of the molecule at room temperature. As a result, the ion mobility will be independent of the electric field and the drift velocity will be directly proportional to the field E.

$$v^{+}_{drift} = \mu^{+} E$$

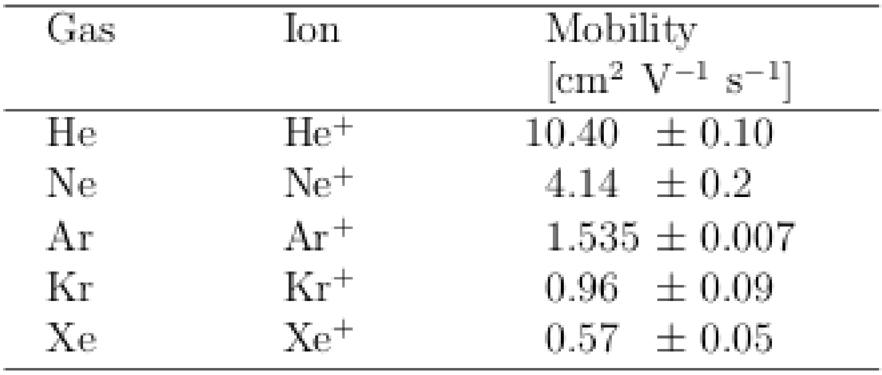

Gas	Ion	Mobility [cm^2 V^{-1} s^{-1}]
He	He$^+$	10.40 ± 0.10
Ne	Ne$^+$	4.14 ± 0.2
Ar	Ar$^+$	1.535 ± 0.007
Kr	Kr$^+$	0.96 ± 0.09
Xe	Xe$^+$	0.57 ± 0.05

Figure 3.2: The mobility of noble gas ions in the parent gas [37]

where v^{+}_{drift} is the ion drift velocity and μ^{+} is the ion mobility. Due to the mass, the drift velocity of the ion will be smaller than that of the electron by an order of 10^{-4}. The mobility of the noble gas ion in the gas is given in table 3.2. However, the ion mobility can change when the ionization is transferred to a neutral atom by the ion. In a gas mixture, both noble gas and quencher will have different cross-sections and ionization can take place by exchange. However, the ion mobility will depend only on the gas mixture and be independent of the electric field.

3.3.3. Drift velocity in Electric and Magnetic fields

In high-energy physics experiments, a magnetic field also will be applied to determine the momentum of the highly energetic particle from the curvature of their trajectories. As both electrons and ions are charged particles, they will be affected by the magnetic field. The drift of these particles in electric and magnetic fields can be described by the Langevin equation by assuming that the mean time τ between the collisions is independent of the E:

$$m\frac{d\vec{v}_{drift}}{dt} = e\vec{E} + e[\vec{v}_{drift} \times \vec{B}] - \frac{m}{\tau}\vec{v}_{drift}$$

here $\frac{m}{\tau}$ is the frictional force proportional to the drift velocity and e, m is the charge and mass of the electron. Solving for $\frac{dv_{drift}}{dt} = 0$ and t is greater than τ will give

$$v_{drift} = e\frac{\tau}{m}\frac{1}{1+\omega^2\tau^2}(\vec{E} + \omega\tau[\vec{E}\times\vec{B}] + \omega^2\tau^2(\vec{E}\cdot\vec{B})\vec{B})$$

Here $\vec{E}$ and $\vec{B}$ are the electric and magnetic field vectors. If the electric and magnetic fields are perpendicular, then the last term in the above equation becomes zero and the direction of the drift will be in the direction of $\hat{E}\times\hat{B}$. However, if the term $\omega\tau$ is very small, then the drift direction will be along $\hat{E}$ and for large values of $\omega\tau$ the drift direction will be along $\hat{B}$. In SCTF TPC, the electric and magnetic fields are parallel, and hence, the magnetic will not affect the drift direction. Even though the applied fields are expected to be homogeneous, they will have small variations and this distortion in the fields can affect the particle trajectory. However, as the drift distance of SCTF TPC is small, such deviation can be neglected.

3.3.4. Diffusion

When drifting along the direction of E, electrons will scatter as a result of their collision with the gas molecule. Electrons in the cluster will have momentum along all directions after a few collisions and as a result, the cluster will diffuse. The transverse deviation of the cluster from its original path due to the collision is called transverse diffusion and the longitudinal deviation due to the same is called longitudinal diffusion. For a conserved electron current $\vec{\Gamma}$, the density distribution of electrons ρ_e satisfies the continuity equation.

$$\vec{\Gamma} = \rho_e v_{drift} - D\nabla_{\rho_e} = constant$$

solving this equation will give a Gaussian distribution with time-dependent width:

$$\rho_e = (\frac{1}{\sqrt{4\pi Dt}})^3 exp(\frac{-r^2}{4Dt})$$

Suppose, if a cluster starts from the origin and drifts towards the z direction, then the square of the distance to the center of the cluster will be $r^2 = x^2 + y^2 + (z - v_d t)^2$ and the width of the distribution at any direction will be:

$$\sigma = \sqrt{2Dt}$$

where D is the diffusion coefficient. As they contribute to the total electron smearing, both transverse and longitudinal diffusions have a significant influence on the particle track reconstruction and spatial resolution.

Anisotropy due to electric and magnetic fields

As the energy will be different for electrons in a cluster, the diffusion will not be isotropic. If the collision cross-section is a function of electron energy (as discussed in the previous sub-section), then this will result in a change in longitudinal diffusion (D_L) and the transverse diffusion will be the same as in the isotropic case. The resulting density distribution of electrons will be:

$$\rho_e = (\frac{1}{\sqrt{4\pi D_T t}})^2 \frac{1}{\sqrt{4\pi D_L t}} exp(-\frac{x^2+y^2}{4D_T t} - \frac{(z-v_d t)^2}{4D_L t})$$

The magnetic field also can induce anisotropy in diffusion. As mentioned earlier, the magnetic field will be parallel to the electric field at SCTF. In this case, the field will not affect the longitudinal diffusion. However, the magnetic field will change the particle trajectory to a helix between two impacts, projecting onto the XY plane with radius;

$$\rho = \frac{c}{\omega} sin\theta$$

Here c is the velocity between two collisions, θ is the angle between its path and the z-axis and ω is the cyclotron frequency. As a result, the transverse component of the motion will be curled up and this will reduce the transverse diffusion:

$$D_T(\omega) = \frac{1}{1+\omega^2\tau^2} D_T(0)$$

3.4. Gas Amplification and Readout

Gas amplification has a crucial role in particle detectors especially when applying large electric fields. With high electric fields, the electrons will get enough energy between collisions to ionize the gas molecules. This will generate additional free electrons and these electrons will undergo acceleration and cause further ionization, resulting in the avalanche effect. This process called gas amplification, is of paramount importance for enhancing the detector sensitivity. The number of primary electrons created by the particle when it passes through the gas mixture can be very small. For example in an argon at atmospheric pressure, the number of electrons will be about 94 electrons per centimeter and if these electrons were distributed across the readout pads, each pad would get very few electrons which is inadequate to achieve a good signal-to-noise ratio using electronic amplification. This is because even the best amplifiers will have an electronic noise in the range of a few electrons. The best solution for this challenge is gas amplification. The gas amplification process can multiply the number of primary electrons by a factor up to 10^6. Through this multiplication process, the detector will be able to achieve a good signal-to-noise ratio which enables the detection of even faint particle interactions.

The number of electron-ion pairs produced per unit length can be calculated using the first Townsend's coefficient α:

$$dN(s) = \alpha(s)N(s)ds$$

for a strong inhomogeneous field of gas amplification, the electric field and the ionization coefficient α depend on s. If the electric field is above the ionization threshold between s_0 and s_1, then the total number of electrons N after the gas amplification created from N_0 primary electrons is:

$$N = N_0 exp(\int_{s_0}^{s_1} \alpha(s)\, ds) = N_0 G$$

where $G = N/N_0$ is called gain.

3.4.1. Multi wire Proportional Chamber

The objective of the proportional wire chamber is to generate a high electric field in the vicinity of a thin wire, called a sense wire or amplification wire. These wires are positioned within the gas volume and the electric field amplitude around the wire will have an inverse relationship with the distance from the wire, indicated by 1/r, where r is the distance to the wire. Moreover, the other two parameters are s_1, the critical radius or the distance from the wire where the electric field gains a substantial magnitude that is capable of the amplification process. This point acts as a threshold above which field strength will be enough for electron amplification and s_2, which is the outer radius of the wire. Near the amplification wire, the electric field line will be perpendicular to the surface of the wire. This implies that the motion of the electrons primarily occurs radially towards the wire. When the charged particle passes through the drift volume by ionizing the gas molecules, the electrons will feel this radial field and move toward the wires. This radial motion near the wire surface will induce avalanches which will lead to a strong charge signal.

As the strength of the electric field increases, the large number of electrons in the inner shells of the atoms can be excited, and as a consequence, photons will be emitted exhibiting a long mean free path capable of initiating additional ionization avalanches. For such scenarios, the resulting signal will deviate from the proportionality with the number of primary electrons and may lead to a continuous amplification process called a streamer. These photons should be absorbed to ensure signal proportionality and a stable operation at high gain factors. This can be achieved by using quenchers such as CO_2 and CH_4 which have high absorption cross sections for photons.

A multi-wire proportional readout can be used as the amplification structure in TPC. A grid of thin amplification wires will be placed near the pad plane while an additional grounded layer represents the anode of the drift space. The high positive potential will be applied to the sense wires. Field wires will be placed alternatively with sense wire in the same plane to ensure field quality in the amplification region. The electrons will be amplified at the sense wires and will induce a signal on the pads. However, the main contributors to the signal are ions moving in a strong electric field near the wire surface. As the ions move slowly compared with electrons, the time scale of the signal generation will be longer.

3.4.2. Micro Pattern Gas Detectors (MPGDs)

Even though proportional wire readouts have been operated successfully for decades, it has several limitations. The unconditional alignment of wires will induce an anisotropy. The minimum spacing between wires is usually a few millimeters which will limit the attainable spatial resolution. Also, holding wires in their position needs, strong tension

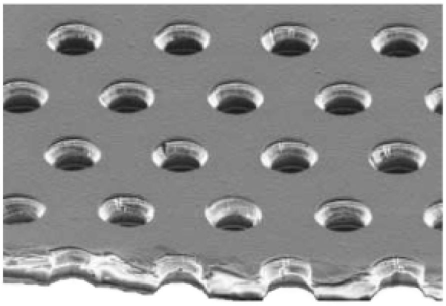

Figure 3.3: Electron microscope picture of a GEM foil [39]

and a rigid support system. Additionally, the intense electric field surrounding the wires deviates from the magnetic field, typically orthogonal to the time projection chamber's (TPC) readout plane, resulting in E×B-induced distortions. Many of these limitations can be avoided by using MPGDs such as MicroMEGAS and Gas Electron Multiplier (GEM). These devices have advanced amplification systems with a pattern of size about $100\,\mu$m.

Gas Electron multipliers (GEM)

The Gas Electron multipliers (GEMs) were first introduced in 1997 by Fabio Sauli at CERN [38]. The Gas Detector Development Group led by him developed a GEM using Kapton foil of $50\,\mu$m thickness and copper coated on both sides. The holes are etched into the foil in a pattern. The pitch in the pattern is in order of a few micrometers. A picture of GEM foil is shown in fig 3.3.

This GEM foil will be placed between drift and charge-collecting electrodes. When a high potential difference is applied between these electrodes, equipotential and field lines will appear near the holes. Due to the large potential difference, a high electric field will form in the holes and as a result, the electrons from the upper region will drift toward the holes and will acquire energy for ionizing collision with molecules of gas filled in the GEM foil. This large number of electrons in the avalanche will move to the bottom of the structure where these electrons will either be collected by an electrode or injected into the next GEM structure. fig. 3.4 shows the electric field shape in the GEM holes. The signal generated in the anode is from the collection of electrons only and this will make

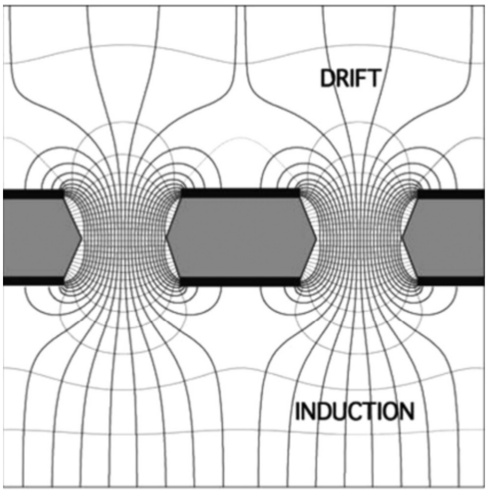

Figure 3.4: Electric field shape in GEM holes [40]

the detector faster. Using multiple GEM structures is the best approach to increase the gain with a risk of discharge. A good example of a multiple GEM structure is Triple GEM. Triple GEM has three GEM structures with a suitable drift gap (usually 1 - 3 mm) and an anode. In SCTF, a detailed simulation study has been done to find the gain in triple and quadruple GEM structures by using selected gas mixtures.

Micromegas

Introduced by Y. Giomataris in 1992 [41], Micromegas is another MPGD widely used for amplification in TPCs. Micromegas is composed of finely woven wire mesh (referred to as micro-mesh) positioned at a short separation distance (approximately 50-100 μm) above a plane of pads. When a potential of several hundred volts is applied between the mesh and pad plane, the amplification will occur in the region. As shown in Fig. 3.5, the mesh will act as anode of the drift region. The electrons drifting towards the micromegas will traverse the mesh and experience amplification due to the high electric field in the region between the mesh and pad plane. Subsequently, the electrons are collected on the pad plane. To ensure consistency in the amplification, the distance between the mesh and the pad plane will remain constant throughout the readout structure. This can be done by using pillars or space grids. The device provides good time resolution as the electron signals are much faster than the induced ion signals of wires.

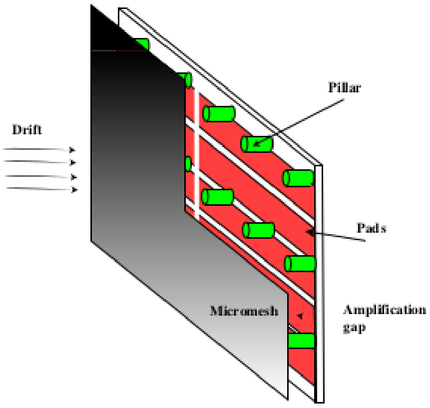

Figure 3.5: Geometry of Micromegas [42]

3.5. Ion Backflow

The amplification process by the readout system of TPC will generate avalanches of electrons and a large number of ions. While the avalanche is absorbed by the bottom electrode, the generated ions will travel in the opposite direction, towards the active volume of TPC. These ions will move towards the cathode and hence, as the drift velocity of ions is several orders of magnitude smaller than that of electrons, they will stay in the drift volume for a long time and this will create a distortion in the applied electric field in the volume. This mechanism is called ion backflow (IBF). Moreover, If the rate of ionization events in the drift volume is too high, such that the ions are generated faster than they can drift out of the volume (because their drift velocity is much slower than the electron drift velocity), the ions will accumulate in the active volume and distort the applied electric field.

3.5.1. Suppression of IBF in GEM

In the first-generation TPCs, a wire mesh with a synchronous gating pulse is placed in front of the active multiplier. However, the gating will not be effective if the event distances are smaller than the drift time. Hence, efforts to reduce IBF have been taken by using specific field configurations in the single or multiple GEM structures. In multiple GEM detectors, a suitable distribution of gain will decrease the IBF. In addition to the gain, IBF has a dependence on the gas mixture used and hole diameter. Moreover, there are many techniques that can reduce the IBF. many of these are discussed in the coming chapters.

3.5.2. Charge transfer in multi-GEM structure

In a multi-GEM structure, the charge transfer depends on the voltage applied across GEM foils and the electric field between the GEMs. In a triple GEM, the field between the first GEM and the second GEM is called $first transfer field$ (E$_{trans1}$). Also, the field between the third GEM and the pad plane is called $induction field$ E$_{ind}$. The important charge transfer parameter for each GEM is, collection efficiency C:

$$C^{\pm} = \frac{N_{e^-I^+} collected to the GEM hole}{N_{e^-I^+} in front of the GEM hole}$$

and extraction efficiency X:

$$X^{\pm} = \frac{N_{e,I} extracted from the GEM}{N_{e,I} in GEM hole}$$

and the gain factor G is:

$$G = \frac{N_e in GEM hole}{N_e collected to GEM hole}$$

The ratio of the number of electrons after the transfer to the number of electrons in front of the GEM is referred to as $effective gain$ G$_{eff}$ and this can be expressed in terms of collection coefficient, gain, and extraction coefficient.

$$G_{eff} = C^- G X^-$$

also, the ion backflow can be calculated as the ratio of the number of ions drifting back to the number of electrons collected in the anode pads. As the collection and extraction coefficients are determined by the voltage across the GEM foil and the magnitude of the electric field on both sides of the foil, these parameters can be optimized by studying the electrostatics of the GEM foil. Unlike Micromegas, Even though the ions produced in the GEM depends on the gain, the number of ions reach the drift volume is more depends on the electric field strength. This is because most of the ions moving back towards the drift volume from the second and third GEM will not reach it because they follow the field lines which end on the surface of the previous GEM.

3.5.3. IBF suppression in Micromegas

The Micromegas detector exhibits a high electric field beneath the mesh, leading to a significant concentration of field lines in the amplification region originating from the mesh. Consequently, the majority of drifting ions tend to follow these field lines, ultimately reaching the mesh. The suppression of ion backflow is influenced by the ratio of electric fields between the drift region and the amplification region. Therefore, as the gas amplification increases, the proportion of ions drifting back decreases.

Chapter 4

Simulation of TPC

In this chapter, we explore Aurora, a software framework designed for the SCTF experiment, explore different inner tracker (IT) choices, and present the algorithms devised for various simulation studies on the TPC, along with the outcomes of these simulations.

4.1. Introduction

The selection and optimization of sub-detectors and their parameters for Super Charm-Tau Detector (SCTD) require a detailed simulation study and study with the prototype of each sub-detector. For this, a dedicated software framework is necessary. Aurora, a software framework developed by a team of experts at BINP is dedicated to simulation and data analysis for SCTD. All the required software is included in this framework. A brief description of Aurora is given in this chapter. Also, the chapter discusses the potential candidates for IT. A brief description of the cylindrical silicon strip detector and cylindrical micro-RWELL detector is given. A detailed simulation study and results of TPC, which is the strongest candidate for IT and our focus of research is also explained. The TPC simulation in our research involves the creation of a TPC geometry with a sensitive volume, event generation, signal generation, and reconstruction of cluster coordinates are explained and their results are given.

4.2. The Aurora

Inspired by the Gaudi framework [43], Aurora is a software infrastructure developed by experts at BINP for the simulation and data analysis of SCTF detectors and data. Aurora framework incorporates much scientific software widely used in high-energy physics experiments. As a software framework, Aurora covers all the aspects of software component interaction at run-time, including configuration, data exchange, and job running. Moreover, semantic versioning is used to introduce the release of the new version. A traditional method is used in the architecture of the framework, which separates code and data. The algorithms process the physics data on an event-by-event basis. The algorithms take input data and produce new data as output through manipulation. For some processes, this may be entrusted to some tools. The framework provides data storage between algorithms.

The algorithms and tools are designed using C++. For configuration and control, python is used. The Scientific Linux 7 at x86_64 architecture, with GCC 9 as the main compiler is used as a computing environment for the framework. The generation of events will be done using a selected generator and then injected into the simulation, yielding the event picture in the detector. The output of the simulation will be processed using digitization modules and, their output data format will be exactly the same as it would be for the real detector hardware. Hence, the reconstruction can be done with either simulated or real (future) data. At each stage of the simulation, the intermediate data can be routed directly from one module to another, or stored and read back later. The details of the software included in the framework are given below.

4.2.1. DD4hep

Developed by a team of experts from CERN and many other institutes, DD4hep is used to simulate the geometry of detectors in high-energy physics experiments [44]. The software provides a full detector description which includes the geometry, materials, visualization, readout, alignment, calibration, etc. In addition, it supports all phases of the detector life cycle: detector concept development, detector optimization, construction, and operation. The software provides an extension to other simulation software such as Geant4, GenFit, etc. Also, DD4hep has minimal dependencies and can be a single source of detector information for simulation, reconstruction, and analysis. In Aurora, DD4hep is used for the construction of TPC geometry with sensitive volume. DDG4, a special tool provided by DD4hep is used to supply the uniformed geometry description to Geant4 and has been used to make the drift volume sensitive. A detailed description of the algorithm used for geometry is given in the section 4.4.

4.2.2. Geant4

Geant4 is one of the most popular simulation software developed by Geant4 collaboration which includes researchers from various institutes [45]. Geant4 is mainly used for the creation of geometry with materials, locating points and navigating tracks in that model, applying the effects of physics interactions and generating secondary particles, and recording selected information either as tallies or create hits (that are used to generate detector response), visualize a setup's geometry and the particle tracks passing through it, and interact with an application via an extensible terminal or graphical user interface. The complete physics process for electromagnetic, strong and weak interactions of particles in matter over an energy range that starts from milli-eV (for thermal neutrons), eV (electrons), or typically keV (hadrons), up to hundreds of GeV (or even in part up to 100 TeV) are included in this software. We used Geant to create a detector response for TPC, which will provide space coordinates and information about time and energy deposition. These Geant4 hits will later convert to raw hits for reconstruction.

4.2.3. GenFit

GENFIT toolkit, initially developed at the Technische Universitaet Muenchen [46], and later extended and modified to be more general for global tracking. It provides many features such as track representation, track-fitting algorithms, and graphic visualization of tracks and detectors, that can be used for any experiment that determines parameters of charged particle trajectories from spacial coordinate measurements. GenFit can perform extrapolations of track parameters and covariance matrices using Kalman filter routines. In our work, a basic algorithm for track reconstruction has been created using GenFit. The details are explained in section 4.8.

Other than this software, ROOT, Garfield, and ACTS are used for data visualization, simulation for readouts, and event reconstruction.

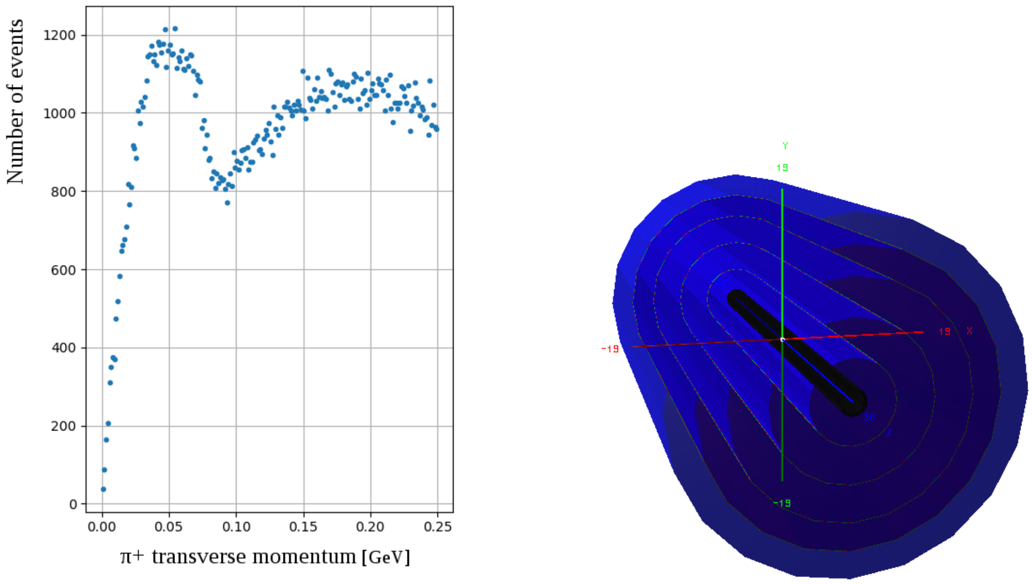

Figure 4.1: a) distribution of π^+ mesons from the reaction $ee^+ \to DD^*$ on their transverse momentum, b) Geometry of four layered Silicon strip detector simulated using DD4HEP

4.3. The Inner Tracker

The basic parameters of IT are discussed in the previous chapter. The important task of IT is the reconstruction of soft hadrons. Simulations were done with DD4HEP[18] and GEANT4[19] packages. The distribution of π^+ mesons from the reaction $ee^+ \to DD^*$ is given in figure 4.4. Pions with different momenta were set perpendicular to the axis of IT. A magnetic field of 1.5T is applied along the beam axis. In the simulation, the beam pipe consists of three layers. Two layers of Beryllium with a width of 1.5 mm each and a paraffin layer of width 0.5 mm. Paraffin is placed between them. The main candidates for the inner tracker for SCTD are the following;

- Four-layer silicon strip detector.
- Cylindrical Micro-Resistive WELL detector (μ-RWELL).
- Time Projection Chamber (TPC).

A detailed description of each candidate is given in the following sections.

4.3.1. Silicon strip detector

The Silicon strip detector (SSD) has four layers of 0.32 mm Silicon and 0.4 mm carbon fiber[47]. Simulation studies show that the minimum momentum required for pions to cross the beampipe is 50 MeV/c. Pions with a momentum of 55 MeV/c can pass the first layer and those with a momentum of 60 MeV/c can pass the second layer. However, pions with momenta 65 MeV/c or more can pass through all four layers in which those with momentum 70 MeV/c return back, and pions with momentum 75 MeV/c cross the layers twice. The simulated geometry of the detector is given in figure 4.1 (b). At present, SSD is successfully implemented in Belle II [48]. The vertex detector of Belle II is a combination of two inner layers of the Silicon pixel detector (PXD) and four outer layers of the Silicon strip detector (SVD). These extended layers of SVD have radii 38 mm, 80 mm, 104 mm, and 135 mm with 7, 10, 12, and 16 ladders respectively in ϕ direction. The double-sided silicon strips and Origami chip-on-sensor readout system are used in the silicon strip vertex detector of Belle II.

Double-sided silicon strip detector is implemented as one of the tracking systems in ALICE [49]. The main tracking system of ALICE is TPC. However, due to high particle density, four innermost layers with silicon pixel detectors and two outer layers of double-sided silicon strip detectors (SSD) were used. The SSD covers 2.3 m^2 in layer 5 and 2.9 m^2 in layer 6. There are 782 and 988 SSDs employed in layers 5 and 6 respectively. ALICE SSD can stand up to 10 krad irradiation. A128C chips are used as readouts for SSD. The power consumption of this A128C is always below 850 μW per channel and 340 μW per channel for a 1 ms readout cycle. Twelve chips were connected with each detector that is, six chips for 768 channels for each side of the detector. All these successful implementations of silicon strip detectors indicate that it will be a good option for the SCTD inner tracker. However, compared with ALICE (5.5 TeV per nucleon pair) and Belle II (10.58 GeV), the Super Charm-Tau Factory has less center of mass energy (2-5 GeV) so the particle produced in SCTF will have less momentum than those produced in the colliders described above. Hence, the internal tracker of the Super Charm-Tau Detector should be very thin otherwise most of the particles will be unable to cross the detector. This limitation will make the construction of silicon strip detectors more

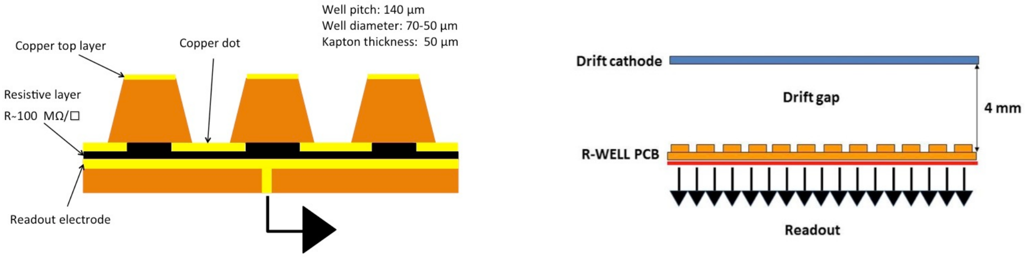

Figure 4.2: Schematic diagram of a) μ-RWELL PCB and b) μ-RWELL detector.

complex and costly.

4.3.2. Cylindrical μ-RWELL detector(C+RWELL)

The micro-resistive WELL (μ-RWELL) is a novel micro-pattern gas detector (MPGD) introduced recently [50] with many advantages over other MPGDs such as gas electron multiplier (GEM) and thick gas electron multipliers (THGEM). Chances for detector damage due to spark is high in MPGDs. This is because of the transition from avalanche to streamer which happens when the size of the primary avalanche exceeds 10^7-10^8 electron-ion pairs. Due to the small distance between the anode and cathode electrode, the streamer can easily followed by a discharge. Another limitation for MPGDs such as GEM and THGEM is the complexity of the assembling procedure. They need time-consuming procedures such as stretching and gluing. Figure 4.2 shows the schematic diagram of μ-RWELL PCB and detector. μ-RWELL is GEM foil etched with a readout PCB plane which is coated with a resistive layer. Copper in the bottom is patterned like copper dots corresponding to each WELL structure. The WELLs have a diameter of 70μm (50μm) at the top (bottom) and a pitch of 140μm. Screen printing technology or technology such as Dimond Like Carbon (DLC) can be used as a resistive layer.

The avalanche formed in the μ-RWELL is collected on the resistive layer through the copper dots and this helps to avoid the formation of discharge and achieve higher gain. Unlike GEM, where the signal is mainly due to the electron motion, the ionic part also contributes to the formation of the signal in a similar way as electrons. Also, it does not need any time-consuming assembly procedures, stretching, gluing, or internal

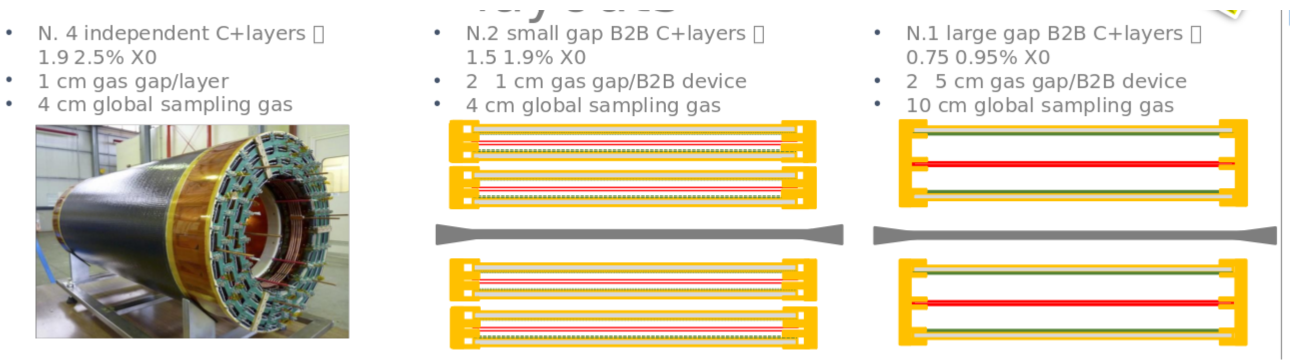

Figure 4.3: Different types of C+μ-RWELL

support frames. The collection efficiency for a particular voltage applied to the WELL structure depends on the drift field. The prototype study shows maximum collection efficiency corresponds to the drift field of about 3.5 keV/cm with maximum achievable gain G > 6000 (ΔV = 525V) which is much higher than the gain obtained by single GEM for which G < 1000 (ΔV = 500V) with same drift field. Even though μ-RWELL has many advantages above other MPGDs, it has some limitations too. The main limitation of μ-RWELL is it cannot stand with high particle flux. At high radiation, the current is drawn through the resistive layer which results in the drop of amplifying voltage. Also, the maximum particle flux that μ-RWELL can able to withstand with the ohmic behavior of the detector decreases with an increase in the diameter of the collimator. Moreover, the character of gain versus particle flux depends on the beam position. Even though μ-RWELL is a better option when compared with other MPGDs.

Three different types of C+RWELL detectors are suggested for inner tracker fo SCTD [52].The geometry of these types is shown in fig 4.3. The first type has four independent layers of C+RWELLs with a 1 cm gas gap per layer. This type of detector has a material budget of about 1.9-2.5 % X_0. The second model has two layers in which each layer has two C+RWELL with a cathode layer in between. Each layer has a drift gap of 2 cm. This model detector has a material budget of approximately 1.5-1.9 % X_0. The third model has the least material budget of 0.75-0.95% X_0 which is half that of the second model. The model has only a single cylinder with a cathode layer between two C+RWELL layers. This detector model has a drift gap of 5 cm between each C+RWELL and cathode layer. However, all these models are in the early stages of study and they need the design, construction, and testing of prototypes. At present, the Cryogenic Magnetic Detector of the VEPP-2000 collider in BINP is developing a C+RWELL detector for its Z-chamber [51]. This is expected to be the first detector of this kind. The geometry of this Z-chamber is similar to the third type described above. The new Z-chamber is a triple cylinder in which a cathode in the center and two μ-RWELL structures as inner and outer cylinders with diameters of 617 mm, 643 mm, and length 550 mm. The μ-RWELL structure is also used in endcap discs of the Z-chamber.

4.3.3. Time Projection Chamber (TPC)

The Time Projection Chamber (TPC) is considered the best option for IT at SCTF. Two sub-options for TPC are considered for Super Charm-Tau Detector. The first one is standard TPC for which the inner and outer walls both have the same width and are made of 1 mm G10, 0.1 mm Teflon, and 15 μm Copper. The second option is TPC with a thin inner wall made of 50 μm Kapton, 0.1 mm Teflon, and 5 μm Copper. The second sub-option is more suitable chosen with a material budget of about 1.4-1.6 % X_0.

4.4. TPC geometry and Event generation

The TPC geometry of both sub-options has been created using the DD4hep software package [44] included in the aurora. A combination of Kapton disk with 1 mm thickness and copper disk of thickness 1mm are used as cathode disks. A mixture of argon with 20% CO_2 is created and this volume in TPC is made as a sensitive volume. The sensitive volume is created using the Genat4. The geant4 will collect the TPC parameters and provide the position coordinates and time for hits created during the event. The decay $D^{*+}D^{*-} \to D^0\pi^+$ and $D^0 \to K^{\pm}\pi^{\mp}$ is created using event generation package and used for simulation. The $D^{*+}D^{*-}$ is created by the decay of $\Psi(4040)$ which is created by the e^+e^- collision. A constant electric field of 15kV and magnetic field of 1.5 T were also applied to the TPC. The electric and magnetic fields are parallel to each other. The gas mixture given can be changed as per the requirement by creating new mixtures in DD4hep.

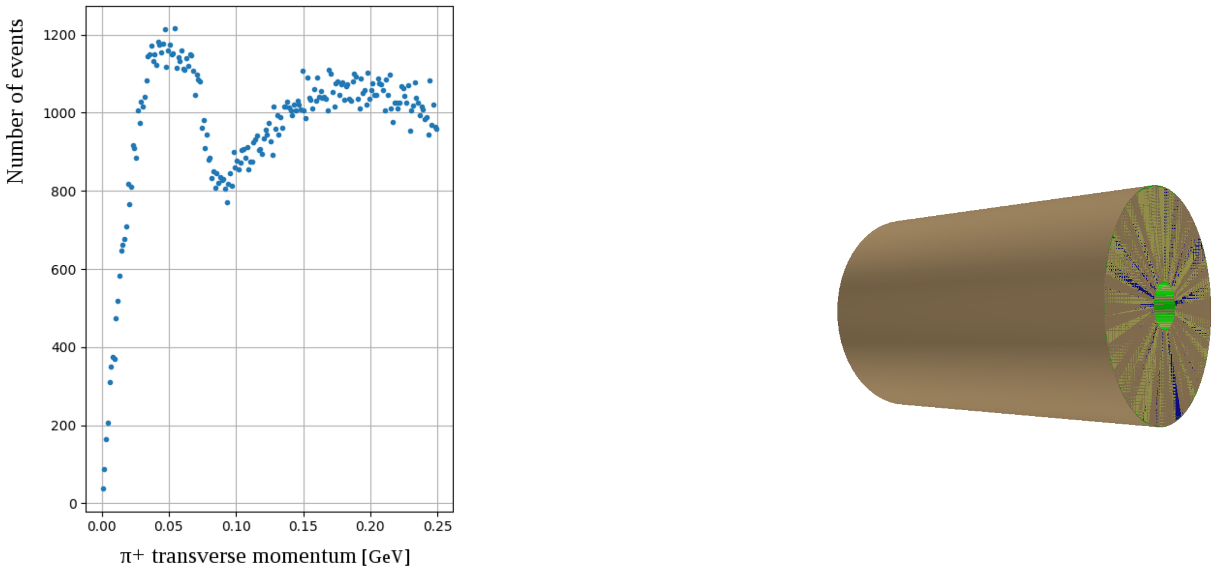

Figure 4.4: a) distribution of π^+ mesons from the reaction ee$^+$ $\rightarrow$ DD* on their transverse momentum (in GeV/c), b) Geometry of TPC with sensitive volume simulated using DD4HEP

The two options of the TPCs discussed above have been used for the study [47]. The main aim of the study was to find the minimum transverse momentum required for the particle to enter TPC. The simualted pions from the decay $e^+e^- \rightarrow DD^*$ is shown in fig 4.4(a). The pions with different momenta are directed perpendicular to the beam axis. The beam pipe in the simulation has 3.00mm of Beryllium and 0.5mm of paraffin. The paraffin is placed between the Bayllium layers of thickness 1.5mm. Argon with 20% of CO_2 is used in this study.

The result of our study is visualized in fig4.5. The pions with momenta less than 55 MeV/c can pass through the inner wall of a thin TPC, but they do not cross the inner wall of the standard TPC. For the standard TPC, the minimum momenta required for a pion to cross the inner wall is found 60 MeV/c. The outer wall of the TPC has also an influence on the path options. In the case of thin and standard TPC, the pion of momenta 60 MeV/c cannot cross the outer wall of the TPC. The pions with momentum greater than or equal to 70 MeV/c cross the outer wall of both thin and standard TPC multiple times and produce soft electrons which can leave a lot of ionization in the volume. Based on the result of these results, the TPC with thin walls is recommended as IT. The main

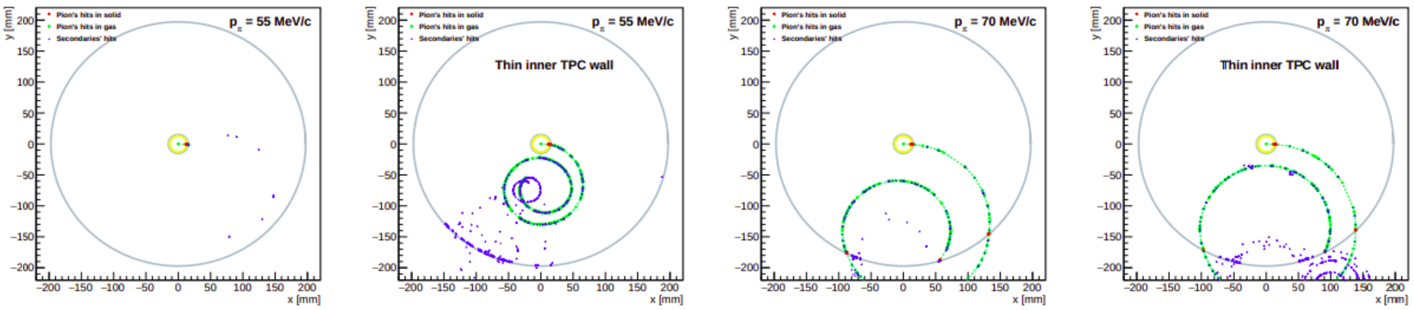

Figure 4.5: Simulation of cross-section on TPC by pions and secondary particles

reason for choosing the thin TPC is it can allow the passage of soft pions. The pions from the decay of DD* mesons will have low momentum shown in fig 4.4 and by using the thin TPC, this pion can be reconstructed.

4.5. Transport parameters of gas mixtures

The gas mixture plays an important role in the measurement of spatial resolution and dE/dX in TPC. The selection of a suitable gas mixture depends on many factors such as transport properties, availability, and cost of the gas mixture. To obtain very good resolution and for successful track reconstruction, it is important to understand the transport properties such as transverse and longitudinal diffusion, drift velocity, and Townsend coefficient of electrons in the gas mixture. A detailed simulation study of transport parameters of electron has been done and results were published [53]. Argon and Neon-based gas mixtures are chosen for simulation studies. The main reasons for the selection of argon and neon are their availability and simplicity of keeping. The study has been done using the Garfield++ software package [54]. The Garfield++ software is a computer program designed for simulation in two and three dimensions. The interface to Magboltz [55] will help to compute electron transport properties in gas mixtures. Also, it has an interface to Heed which is a program that allows to simulation of ionization of gas molecules by particle traversing the chamber. The properties of some gases are given in table 4.1. From the table, it is clear that argon has a high density and electron-ion pair for a minimum ionizing particle with the least radiation length. Besides the gases given in the table, iC_4H_{10} is also used for studies.

Gas	ρ [g/l]	X_0 [g/cm^2]	X_0 [m]	N_t [1/cm]
He	0.1785	94.32	5280	8
Ne	0.8999	28.94	322	40
Ar	1.784	19.55	110	97
CH_4	0.717	46.22	645	54
CO_2	1.977	36.2	183	100
C_2H_6	1.977	45.47	335	112
CF_4	3.93	36	90	120

Table 4.1: *Properties of commonly used primary and quenching gases at normal temperature and pressure. Density ρ, radiation length X_0, total number of electron-ion pairs for MIPs N_t.*

The mixtures of argon and neon with other gases in various propositions are created using the software package. The gas mixtures are created in 200 V/cm and 500 V/cm. The maximum electric field is limited to 500 V/cm to avoid complexity in the construction of the field cage. The diffusion and drift velocity of electrons in selected gas mixtures were studied carefully.

There is no specific rule to choose a gas mixture for TPC. The selection of gas mixture largely depends on the chemical stability, ionization density, radiation thickness, electron drift velocity, diffusion, and quenching properties of the components. The study of transport properties of electrons in neon and argon-based gas mixtures has been done to choose a suitable gas mixture as a drift medium in TPC. The transverse and longitudinal diffusion and drift velocities were studied. The variation of diffusion with applied electric field is studied and the results were published [53]. A comparison of variation of transverse and longitudinal diffusion in some argon and neon-based mixtures is shown in fig 4.7. From the figure, one can see that in general, the diffusion coefficient in neon based gas mixtures is less than most of the argon based mixtures. In argon based mixtures, argon with 10% CO_2 and argon with 10% have highest diffusion coefficient for transverse and

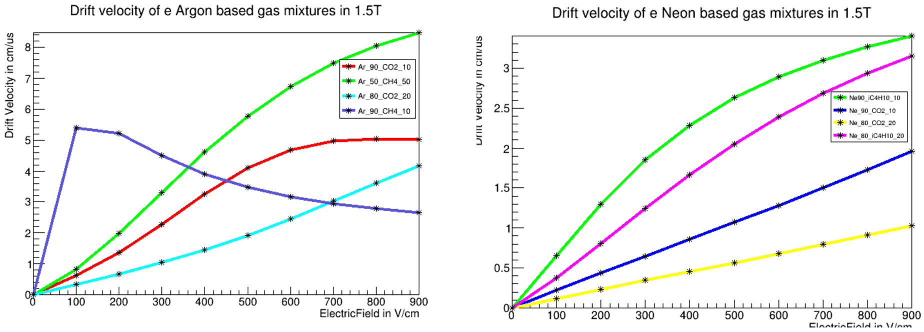

Figure 4.6: *Drift velocity of electrons in a) Ar-based gas mixtures b) Ne-based mixtures*

longitudinal diffusion. Moreover, the general trend is, diffusion coefficient decreases with an increase in the applied field. However, in the case of transverse diffusion, Ar-CO_2(10%) and Ar-CH_4(10%) show different behavior. While diffusion increases with the increase in the applied field in Ar-CH_4 (10%), the diffusion shows a decrease till 400 V/cm and then shows a sharp increase with the applied field in Ar-CO_2(10%).

Other than diffusion, the drift velocity of electrons also highly depends on the gas mixture used. The TPC for the inner tracker should be able to provide drift velocity not less than 5 cm/μs. The lower the drift velocity, the higher the track overlapping which will make track reconstruction complicated. Fig 4.6 shows the drift velocity of electrons in some argon and neon-based gas mixtures. The studies show that the electrons have 3 times higher drift velocity in argon-based mixtures when compared with neon-based mixtures and neon requires a high electric field to get drift velocity which will increase the cost and make the construction of the field cage more complicated. Hence, the argon based gas mixture is more favorable for inner tracker TPC and we considered argon based mixtures for further simulations. In the fig 4.6, one can see that, When drift velocity in all other argon-based gas mixtures increases with the applied field, Ar-CH_4 (10%) has a different character. This is because the total cross-sections in Ar and CH_4 are very similar to each other. Both have dips in cross sections at the same energy, about 0.3 eV. The only difference is that in Ar, the depth of this dip is three times larger. It means that an electron will speed up even at the relatively small electric field until it reaches the minimum in the cross-section. That explains why this mixture has such a relatively high velocity at small electric field tension. When there is an increase in the electric field tension, the cross-section will rise quickly and a drifting electron will move slower. However, if the proportion of methane increases, the dip becomes more shallow and this effect first becomes less pronounced and then disappears. Due to this behavior, it is possible to achieve a drift velocity of 5.3 cm/μs in Ar-CH_4 at 125 V/cm and this will simplify the construction of the field cage. However, the methane gas is highly inflammable and the use of it can increase the risk of spark. Although from the figure, it is also clear that the drift velocity of Ar-CO_2 is less than the required velocity, hence a further simulation is done to find suitable argon-based gas mixtures. The diffusion and drift velocity of electrons in more argon-based mixtures are given in table 4.2 and 4.3. The studies are done in both 200 V/cm and 500 V/cm. From the table, one can see that there are many argon-based gas mixtures that can provide a drift velocity above 5 cm/μs even in a field of 200 V/cm.

gas mixture	D_t in $\sqrt{cm}$	D_l $\sqrt{cm}$	v_d cm/μs
Ar-(10%)CF_4	0.00385	0.0190	7.70
Ar-(20%)CF_4	0.00369	0.0161	6.70
Ar-(50%)CF_4	0.00382	0.0169	5.82
Ar-(10%)CH_4	0.01360	0.0312	5.22
Ar-(20%)CH_4	0.00790	0.0296	7.10
Ar-(50%)CH_4	0.00617	0.0343	6.80
Ar-(10%)CH_4-(5%)iC4H10	0.01000	0.0300	5.01
Ar-(5%)iC4$H_1$0-(10%)CF_4	0.00540	0.0211	5.14
Ar-(15%)CF_4-(5%)CH_4	0.00400	0.0200	6.56
Ar-(10%)CF_4-(10%)CH_4	0.00430	0.02120	6.72

Table 4.2: diffusion and drift velocity in different argon-based mixtures at 200 V/cm

In our studies, we found that, in general, the Ar-CF_4 and Ar-CH_4 mixtures can provide high drift velocity in a low electric field [56]. The transverse diffusion in these mixtures is also small compared with gas mixtures mentioned in fig 4.7. At 200 V/cm, electrons have a high drift velocity of 7.7 cm/μs in Ar with 10% CF_4 followed by a mixture of argon with 20% CH_4 in which velocity is 7.1 cm/μs. In all other mixtures, the drift velocity is less. The study also indicates that adding a small proportion of CF_4

Gas mixture	D_t in cm/$\sqrt{cm}$	D_l cm/$\sqrt{cm}$	$v_d cm\ /\mu$s
Ar-(10%)CF_4	0.00651	0.0123	11.4
Ar-(20%)CF_4	0.00440	0.0111	10.7
Ar-(50%)CF_4	0.00400	0.0100	9.20
Ar-(20%)CH_4	0.02110	0.0181	5.70
Ar-(50%)CH_4	0.01020	0.0172	9.14
Ar-(40%)CF_4-(15%)iC4H10	0.00670	0.0123	5.53
Ar-(5%)iC4$H_1$0-(10%)CF_4	0.00650	0.0142	9.13
Ar-(15%)CF_4-(5%)CH_4	0.00470	0.0123	10.89
Ar-(40%)CF_4-(15%)CH_4	0.00450	0.0111	8.53
Ar-(15%)CF_4-(40%)CH_4	0.00500	0.0136	9.01
Ar-(10%)CF_4-(10%)CH_4	0.00620	0.0125	11.1

Table 4.3: Diffusion and drift velocity of electrons in different argon-based mixtures at 500 V/cm [56]

or CH_4 to other gas mixtures can increase the drift velocity. In addition, increasing the proportion of CF_4 and CH_4 above 50% will decrease the drift velocity of electrons. The drift velocity in all mixtures of argon with or containing CO_2 is very small ($\lessapprox$ 4 cm/μs) and these mixtures cannot be used. The trend of increasing drift velocity with applied electric field continues for all gas mixtures other than the mixture of argon with 10% CH_4 at 500 V/cm. The electron can achieve a drift velocity of 11.4 cm/μs in the mixture of argon with 10% CF_4. However, the change in diffusion is comparatively small in almost all gas mixtures. In brief, the mixtures of argon with CF_4 and CH_4 are the most suitable gas mixtures for inner tracker TPC. The mixture of argon with i$C_4H_1$0 can also be used by adding a small fraction of CF_4 and CH_4. However, finalizing a gas mixture depends on many other factors such as avalanche gain, transverse resolution, etc. These are explained in the next chapter.

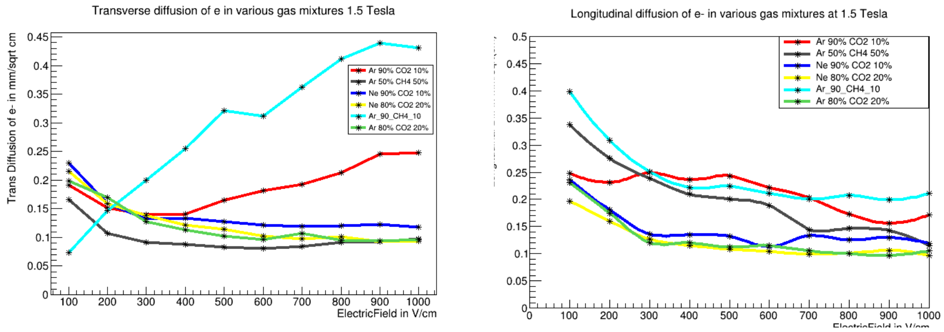

Figure 4.7: diffusion of Ar and Ne-based gas mixtures in 1.5 T magnetic field a) transverse b) longitudinal [52]

4.6. Signal generation and reconstruction of track coordinates

The simulation using the TPC geometry with a sensitive volume provides the position coordinates of Geant4 hits created in the sensitive volume with the energy deposited along with the time at which the hit is created in each point. However, the situation is different in the real-time experiment where the output will be the signal with time from which the coordinates should reconstruct for each track. To make the simulation realistic, basic algorithms to generate signals from the raw hits and reconstruct the cluster coordinates from the signals have been built, and the real cluster coordinates and the reconstructed cluster coordinates are compared [56]. The pad size is taken as 1 mm, the pad pitch is 200 microns, the time stamp of ADC time is 50 ns, the avalanche amplification of triple GEM is taken as 100000 and the sigma of avalanche (length of avalanche) is taken as 300 microns. The gas mixture used in this simulation is argon with 10% CO_2. The reconstructed X, Y, and Z coordinates of clusters generated by pions of transverse momentum 1 GeV/c are shown in Fig 4.8. The present state of the reconstruction algorithm works well for single events. For, multiple events, the algorithm needs to develop for grouping of clusters to identify the track to which belongs.

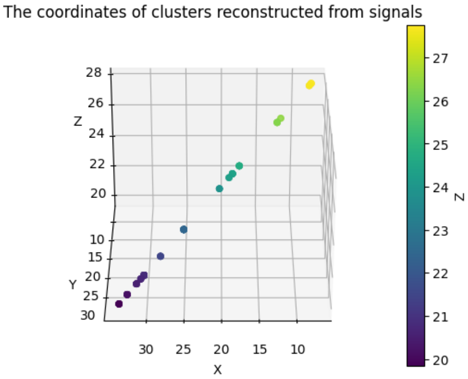

Figure 4.8: The visualization of cluster coordinated reconstructed from signals [55]

Chapter 5

Simulation of Readout system for TPC

5.1. Introduction

The performance of TPC in SCTD heavily depends on its readout system. In our study, we considered different combinations of MPGDs as readout detectors of TPC. This chapter discusses the different options for the readout system of TPC, a GEM-based readout system, and a combination of GEM and micro-RWELL detectors. A brief summary of these options and the results of a detailed simulation study with the triple GEM are given in the following sections.

5.2. Readout System

Micro Pattern Gas detectors (MPGD) with pads are proposed for the readout system. The main task of MPGD is to collect the drift electron and produce an avalanche. This avalanche will create a weak signal which will be amplified and digitized using an electronic system. The main candidates for end-cap detectors are triple GEM and μ-RWELL. The main factors considered in choosing the readout system are field distortion due to Ion Back Flow (IBF), avalanche size, resolution, ability to stand with high particle flux, and cost. Gas Electron Multiplier (GEM), the primary choice for the readout detector has have proven track record as a readout detector for TPC in many experiments such as ALICE, ATLAS, etc. However, the micro-RWELL is a new kind of MPGD which is not yet used as a readout detector.

As discussed in the previous chapter, the micro-RWELL detector is simpler than triple GEM. Unlike other MPGDs, the presence of a resistive layer between WELL and readout PCB helps to avoid the formation of spark and obtain high gain. The first prototype of μ-RWELL based end-cap discs is constructed and tested in BINP for the upgrading of the Z-chamber of CMD3 detector at VEPP-2000 collider [51]. Two prototypes, μ-RWELL and a combination of μ-RWELL with GEM are tested. The study was conducted with different gas mixtures. The test of both prototypes provides a gain value close to the maximum gain that a single μ-RWELL can produce. The prototype of the μ-RWELL-GEM detector provides ten times higher gain than a single μ-RWELL. However, The micro-RWELL has a serious disadvantage as it cannot stay for a long time with high particle flux. Hence, this option needs a more detailed study to check whether it matches SCTD inner tracker requirements.

5.3. The triple GEM Readout system

A simulation study has been done to find the transverse resolution and ion backflow at various argon-based gas mixtures. GEM with field map has been created using COMSOL software package [57], Gmsh [58], and Elmer [59]. The avalanche gain and sigma for avalanche distribution for argon-based mixtures are collected from the simulation and are used to find the transverse resolution. Simulation to study space charge distortion in argon and neon-based mixtures is also done using the field map created using COMSOL. The GEM holes have upper and middle radii of 70 μm and 50 μm and an electric field is applied along the GEM stacks.

The triple GEM is a detector with three GEM foils with a transport gap of 1 mm and an induction gap of 1.5 mm (between the GEM foil and readout structure). One of the main limitations of this detector is electric field distortion in drift volume due to Ion Back Flow (IBF). The IBF is when electrons drift through the hole, it will ionize the atoms of the gas mixture and a portion of ions formed in this ionization will enter the drift volume of TPC. These ions which move slowly, will stay in the volume for a long time and distort the drift field. The IBF depends on the field inside the drift and transfer gaps, the field in the holes, and the hole diameter, and possible to obtain about 10% of all ions produced easily. However, with four GEM cascades of different hole diameters and different applied fields across the GEMs, it is possible to reduce IBF up to 1% [60]. For the estimation of space charge density, results from physics background simulation [61] are used. The calculation of electric field distortion is based on the values obtained for the space charge density with 1% IBF and a gain of 10000. The space charge density is about 10^7 e cm^{-3} near the beam pipe inside TPC and about 10^4 e cm^{-3} near the outer wall of

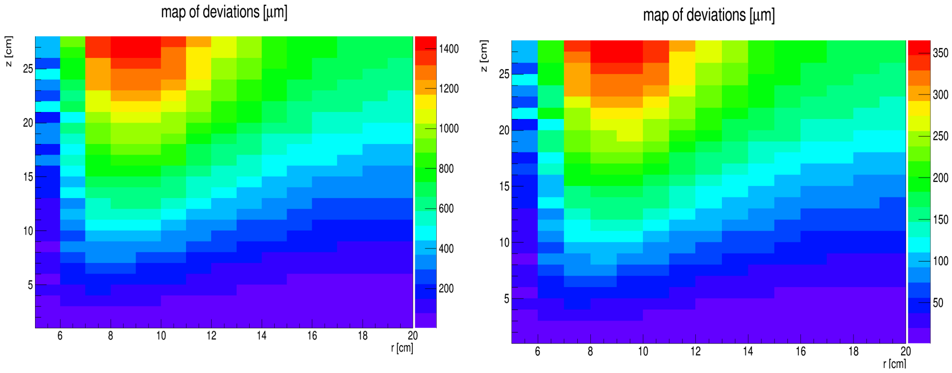

Figure 5.1: *Ion Back Flow in a) Argon and b) Neon*

TPC. The electric field line deviation from the straight line for Argon and Neon-based mixtures is given in figure 5.1. The distortion of the drift field will affect the particle trajectories in the drift volume. The COMSOL simulation package is used to create the field map for the simulation study of field distortion due to space charge. The studies show that the space charge in Ar-based mixtures is four times higher than in Ne-based mixtures. This is because of the higher ionization rate and lower ion drift velocity in Ar. However, these deviations of drift lines are comparable to transversal diffusion and can be compensated in the offline analysis. Hence the argon-based mixtures are used for further simulations.

5.3.1. Ion backflow in Argon-based gas mixtures

The aim of the simulation was to find a gas mixture in which IBF is less than or equal to 1%, and variation of IBF with applied electric field. the gas mixtures argon with 50% CF_4 and argon with 40% CF_4 and 15% CH_4 are used for our simulation. In this study, the GEM geometry and the field maps are created using Gmsh and Elmer. A visualization of the field lines through a GEM hole and the drift of electrons and ions through the GEM hole are given in fig 5.2. In this simulation, the induction and transfer gaps are taken as 2 mm. We used two different kinds of GEM geometries for the simulation, standard GEM and ALICE GEM. For the standard GEM, upper /lower hole diameters are 70 and 50 microns, and the pitch (distance between two nearby holes) is 140 microns. For the ALICE GEM, the hole diameters are the same and the pitch is increased to 280 microns. The ALICE GEM is a special GEM used in the AICE experiment in which the quadruple

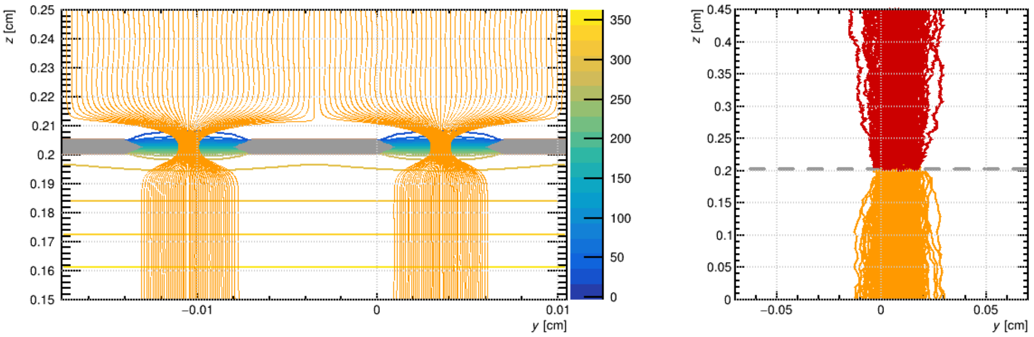

Figure 5.2: The visualization of a) field lines in GEM hole b) drift of electrons and ions through GEM holes (the yellow lines are electrons and red lines are ions moving back)

readout system is used as a combination of standard and special GEM stacks to reduce ion backflow and they successfully reduced IBF to 0.7% [?].

We conducted a simulation study for two different kinds of triple GEM readouts to find the difference in IBF at different applied electric fields. The results of our simulations are given in fig 5.3. From the results, one can see that the IBF increases with increasing field. This is because, at a high electric field, more ions will be produced. Also, due to high drift velocity, the number of ions moving back will increase. At 85 kV/cm, The IBF in argon with 50% CF$_4$ and argon with 40% CF$_4$ and 15% CH$_4$ are 3 % and 3.1% for triple GEM with standard pitch and 2% and 2.1% with a triple GEM in which the first and third GEM stacks are standard GEM and the middle GEM stack is the special GEM. It is noteworthy that the IBF level obtained in our simulation is substantially high when compared with the IBF obtained in the ALICE TPC readout system [?]. This is intentional because, due to the smaller TPC size, the higher space charge density does not lead to significant distortion of the tracks. In ALICE, a quadruple GEM readout system is employed, complemented by a gas mixture based on neon, while we choose triple GEM to make the read system simpler while keeping the same overall gain. Moreover, the voltage configuration within the ALICE GEM readout system follows a specific scheme: $\Delta V_{GEM1} > \Delta V_{GEM2} < \Delta V_{GEM3} \leq \Delta V_{GEM4}$, a scheme designed to minimize IBF. A substantial portion of the ions entering the drift volume mainly originates from ionization events occurring at the first GEM layer. While this can be mitigated by applying a lower voltage across the initial GEM layer, such an adjustment comes at the cost of

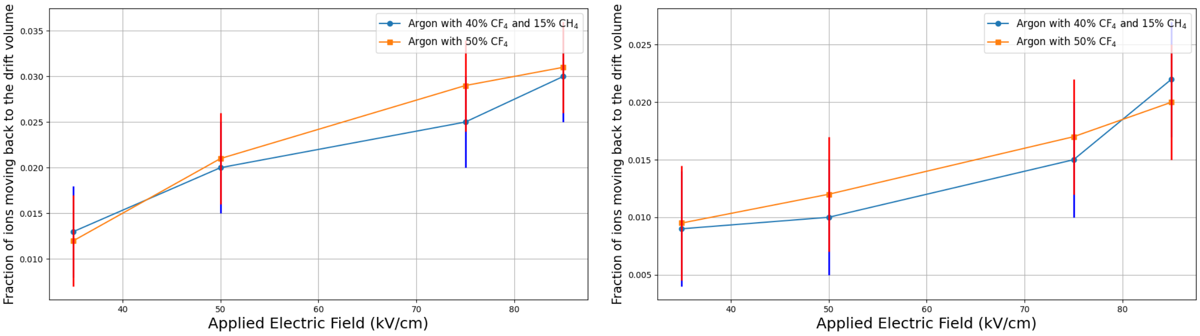

Figure 5.3: Fraction of ions moving back to the active volume at different electric fields for a) standard triple GEM and b) triple GEM as the combination for GEM foils with different pitches. correction: Applied electric field in V/cm

reduced ionization efficiency. Additionally, optimizing material properties and transfer gaps represents another avenue for IBF reduction.

5.3.2. Gas gain in Argon-based gas mixtures

The mean free path is the average distance traveled by the electron between two ionizing collisions. The inverse of the mean free path is the number of ionizing collisions per centimeter, the first Townsend coefficient α. The gas gain depends on the first Townsend coefficient. If n_0 is the number of primary electrons without amplification in the uniform electric field, and n is the number of electrons after the drift distance x in avalanche conditions, then n is given by n $= n_0 e^{\alpha x}$ and the gas gain G is given by G $=$ n_0/n $= e^{\alpha x}$. The first Townsend coefficient depends on the gas mixture, applied electric field, and the pressure. All the above-mentioned parameters are studied using Garfield++ software. For all argon-based gas mixtures, it is observed that the Townsend coefficient increases with an increase in the applied electric field. the result of the simulation for a few gas mixtures is given in 5.4. It is clear from the figure that the Townsend coefficient is increasing with the applied electric field and the chosen gas mixtures, argon with 50% CF_4 and argon with 40% CF_4 and 15%CH_4 which are the most favorable gas mixtures, can provide required gain at high electric field.

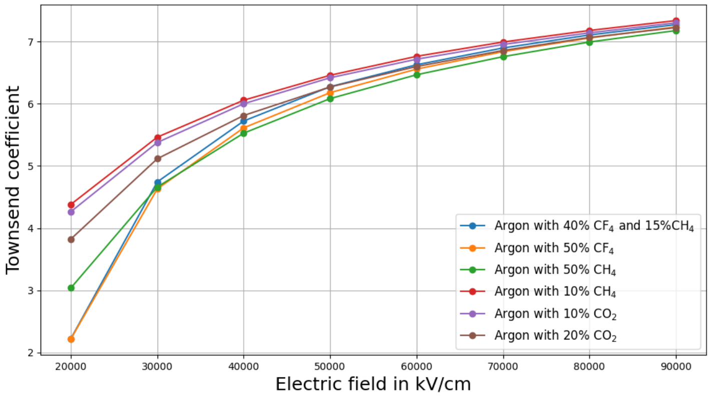

Figure 5.4: change Townsend coefficient with applied electric field in different gas mixtures (correction: applied electric field in V/cm).

5.4. Spatial resolution

The performance of TPC heavily depends on the spatial resolution, which is a combination of transverse and longitudinal resolutions. The main factors affecting the resolution are the gas mixture used, applied electric field, cluster density, gas gain, etc. The transverse resolution, longitudinal resolution (Z resolution) should be less than 200 microns and 700 microns and the spatial resolution should be less than or equal to 1 mm. A detailed simulation study to find the transverse resolution for the tracks parallel and inclined to the beam axis has been done using the Garfield++ package [56]. The tracks parallel to the beam (Z) axis will help to get the best possible resolution. However, in the real-time experiment, almost all tracks will make some angle θ with the beam axis and this explains the need for the study of the resolution of inclined tracks. The Garfield interface to the Heed program is used to create the tracks and the transverse resolution in argon-based gas mixtures is calculated in both 200 V/cm and 500 V/cm. The results obtained from the study of transport parameters are used in this study.

The simulation used the charge centroid method to calculate the transverse resolution for the tracks. Tracks parallel and inclined to the beam (Z) axis have been simulated in our study. The resolution is calculated by finding the difference between the initial XY coordinates of the cluster and the XY coordinates of the center of readout pads. The pads with sizes 700 μm, 1 mm, 1.5 mm, 2 mm, and 3 mm are chosen for the study. The pixel pitch (distance between the nearest pixels) is taken as 200 μm and the distance between the center of the pads is 1.5 mm. A piece of track with a length of 2 mm created by the π^+ with momentum 1GeV/c has been taken for our studies. The interface to HEED is used to create the track piece. The initial coordinates of the track are given using a uniform distribution with limit -a and +a, where a = pixel size + pixel pitch. The resolution for the normal tracks is calculated using the equation:

$$\sigma = \sqrt{\sigma_x^2 + \sigma_y^2} \tag{5.1}$$

here σ_x and σ_y are the resolution of the X and Y coordinates and calculated using the charge centroid method

$$\sigma_x = \sqrt{x_{reco}^2 - x^2} \; and \; \sigma_y = \sqrt{y_{reco}^2 - y^2} \tag{5.2}$$

with x_{rec} and y_{rec} are the XY-coordinates reconstructed using the equation

$$x_{rec} = \sum \frac{X_i q_i}{q} \; and \; y_{rec} = \sum \frac{Y_i q_i}{q} \tag{5.3}$$

x_i, y_i and q_i in the above equations are the X, Y coordinates and charge of the i^{th} pad, and q is the total charge. The charge in each pad is calculated using the expression‘

$$q_i = q \times A \tag{5.4}$$

where q is a constant and A is the size of the avalanche. The term q is calculated using the relation

$$q = C \times P_i \tag{5.5}$$

where C is correction coefficient which is calculated by C = $\frac{1}{\sum_i P_i}$ and P_i is probability of the i^{th} pad is to be fired. As the avalanche distribution is Gaussian, The probability P for a pad is calculated by multiplying the probability of distribution along the X direction with the probability along the Y direction. The probability along the X and Y direction is calculated as $P_x = \Delta f(x)$ and $P_y = \Delta f(y)$ where the terms f(x) and f(y) are the cumulative distribution functions (CDF) of normal distribution and calculated by

$$f(x) = 0.5[1 + erf(\frac{x - \mu_x}{E})] \; and \; f(y) = 0.5[1 + erf(\frac{y - \mu_y}{E})] \tag{5.6}$$

and $P_x = \Delta f(x)$ and $P_y = \Delta f(y)$ are the difference between CDF at the sides of the pads. the mean μ_x and μ_y are taken as the X and Y coordinates of the avalanche center.

In our simulation, the gas mixtures in which the average number of electrons per cluster is 3 or more are preferred as there is a high probability that the cluster may lose in the drift volume due to diffusion if the number of electrons per cluster is very small. The sigma of avalanche distribution is taken as 0.03, gain as 10000, amplification of noise as 2000, and the size of the readout pad as 700 microns. In our simulation, we observed that, out of the gas mixtures we tested, only in argon with 10%iC4H10 and 5%CF_4, the transverse resolution is less than 200 microns. However, the longitudinal resolution in this mixture is above 1 mm, hence omitted. The transverse and longitudinal resolutions measured at 500 V/cm are given in table 5.1. In the table, one can see that the transverse resolution is less than 200 microns in the mixtures Ar with 50%CF_4, Ar with 40% CF_4 and 15% iC4H10, Ar with 40% iC4H10 and 15% CF_4, and Ar with 40% CF_4 and 15% CH_4. however, in these mixtures only Ar with 50%CF_4, and Ar with 40% CF_4 and 15% CH_4 provide longitudinal resolution less than 700 microns.

Table 5.1: *Resolution of parallel tracks in different argon-based gas mixtures at 500 V/cm*

Gas mixture	σ_t (μm)	σ_l (μm)
Ar-(10%)CF_4	273	732
Ar-(20%)CF_4	202	673
Ar-(50%)CF_4	131	619
Ar-(40%)CF_4-(15%)iC4H10	154	732
Ar-(40%)iC4H10-(15%)CF_4	194	850
Ar-(5%)iC4$H_1$0-(10%)CF_4	258	829
Ar-(15%)CF_4-(5%)CH_4	246	732
Ar-(40%)CF_4-(15%)CH_4	178	673
Ar-(15%)CF_4-(40%)CH_4	252	798
Ar-(10%)CF_4-(10%)CH_4	291	743

The variation of resolution with pad size and the drift distance of the clusters are studied to optimize the pad size and to understand the variation of resolution with

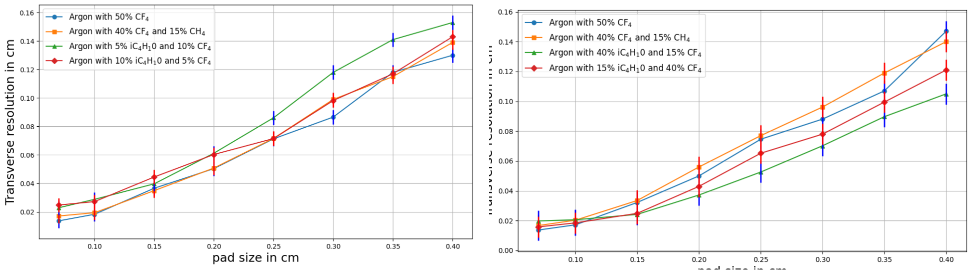

Figure 5.5: *Cluster resolution in different pad size at a) 200V/cm and b) 500V/cm in different Ar based gas mixtures*

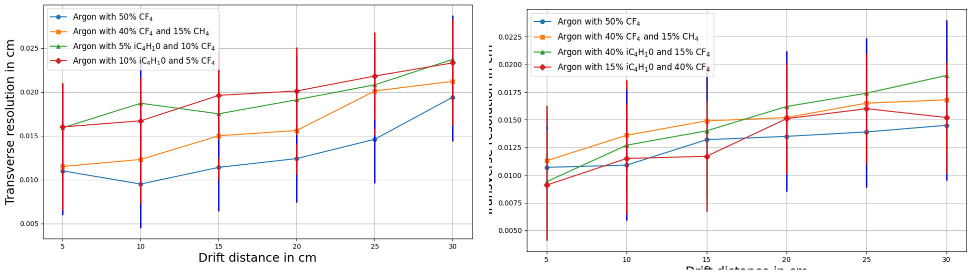

Figure 5.6: *Cluster resolution in different drift distance at a) 200V/cm and b) 500V/cm in different Ar based gas mixtures*

distance. The studies are done at both 200 and 500 V/cm and the results are given in fig 5.5 and fig 5.6. In fig 5.5, it is clear that the best possible pad size is 700 microns and above which, one can't obtain the required resolution. Also, fig 5.6 shows that the resolution gets better with the decrease in drift distance This is because the smaller the drift distance lesser the diffusion.

Chapter 6

Results and Conclusion

Super Charm-Tau Factory, with its rich physics program, is expected to be able to provide more information about c-quarks, charmed mesons, and baryons and able to explain some phenomena that standard models cannot explain such as lepton flavor violation, and CP violation. However, such a rich physics program needs a universal magnetic detector with good accuracy. The Super Charm-Tau detector system involves a vacuum chamber followed by the Inner tracker, Drift chamber, Particle identification system, electromagnetic calorimeter, and muon system. The inner tracker of SCTD will play an important role in the measurements of SCTD as it is placed near the interaction point. The inner tracker should be able to stand with high particle flux. The main task of IT is to register short-lived particle's decays such as $D^{*+}D^{*-} \to D^0\pi^+$ and $D^0 \to K^+\pi$. TPC is considered as a good option for IT and our study focused on optimizing TPC parameters of TPC.

The SCTF project involves a software framework called Aurora to conduct simulation studies and data analysis. Aurora incorporates many software such as Geant4, DD4HEP, ROOT, etc. We did a detailed simulation study of GEM-based TPC have been done in the Aurora framework. Our study aimed to create TPC geometry with sensitive volume and propose a suitable gas mixture in which transverse resolution should be less than 200 microns with minimum IBF. We also aimed to achieve these goals in the minimum possible electric field so that the construction of the field cage could be kept simple. Also, the simulation packages for signal generation from the geant4 hits and reconstruction of the track are done.

6.1. Conclusion

The main results of this research work are listed below:

- A simulation package is developed in Aurora for Optimizing the parameters of TPC.

- Two b options for TPC were proposed for the inner tracker from which the TPC with the thinner wall made of 50 μm Kapton, 0.1 mm Teflon, and 5μm Copper has been selected as the soft pions with transverse momentum of 55 MeV and above can cross the wall of TPC. This is important as the pion from the DD^* will have low momentum. Also, this TPC geometry with sensitive volume is used for event generation and visualization.

- As there is no specific rule to select gas mixture, we proposed argon or neon-based gas mixtures as drift medium for the SCTF TPC. This is because of the availability and easiness of handling. The range of the applied electric field is restricted from 100 to 1000 V/cm to reduce the complexity of the field cage. Our study found that argon is more suitable as electrons can achieve drift velocity 3 times larger than that in neon. Small drift velocity can lead to track-overlapping which will make track reconstruction very difficult. We also noted that IBF is high in argon but this can be compensated with offline analysis.

- To find a gas mixture to achieve the transverse resolution of less than 200 micrometers, we tested several argon-based gas mixtures to find one that can meet the required level of resolution and IBF. We developed an algorithm to measure the transverse resolution using the center of gravity method and tested it with different argon-based gas mixtures. the resolution study has been done for the tracks that are parallel and inclined to the Z axis. Our study found that the mixtures argon with 50% CF_4, and argon with 40%CF_4 and 15% CH_4 meet the requirements of the inner tracker with small diffusion coefficients, high drift velocity, and transverse resolution less than 200 microns. Also, these mixtures have a Townsend coefficient above 6 which proves that it is possible to achieve the required gain with these mixtures. Also, our study found that the readout pad size should be less than 1 mm to achieve the required resolution.

- Digitization package has been built to mimic the real-time detector response. This package will provide the signal in each readout pad with time. The information obtained from the digitization will be used to reconstruct the cluster coordinates and the time of cluster formation. A basic reconstruction package has been built in AURORA for a single event and tested successfully. These packages will help to understand the real-time detector response and the reconstruction package can be used for real-time data analysis after modification.

- In the simulation to measure IBF, we created two different kinds of GEM geometry and field maps using Elmer and Gmsh. The first kind of GEM called standard GEM has a pitch of 140 microns, and the second kind named special GEM has a pitch of 280 microns. the simulation IBF in two kinds of triple GEM readout systems were studied. In the first type, only standard GEM stacks were used and the other one was taken as a combination of standard and special GEM stacks. The electric field range proposed for the readout system was 10 to 100 kV/cm. our study proposes to use a combination of standard and special GEM for the readout system to reduce the IBF to 2% or less.

Our study introduced a novel TPC with argon with 50% CF_4, or argon with 40%CF_4 and 15% CH_4 as drift medium and a combination of standard and special GEM for the readout system for the inner tracker of Super Charm-Tau detector. This TPC can meet all the requirements of the inner tracker. Our TPC is the first small TPC with a continuous readout system operating in an e^+e^- collider. The TPC can provide transverse resolution below 200 μm with an applied electric field 500 V/cm with IBF about 1%. However, a prototype study is essential to finalize these findings. This thesis presents only the main results. The studies conducted with the simulation model are published in the following articles.

List of articles

- TV Maltsev, LI Shekhtman, AV Sokolov, VK Vadakeppattu *Simulation of different options of the inner tracker for Novosibirsk Super Charm-Tau factory detector* EPJ Web of Conferences, **212**, 01011, https://doi.org/10.1051/epjconf/201921201011
- V.K. Vadakeppattu et al 2020 JINST 15 C07021 *Time projection chamber as inner tracker for Super Charm-Tau factory at BINP* Journal of Instrumentation 15, **15(07)**, C07021, 2020, 10.1088/1748-0221/15/07/C07021
- AV Sokolov, TV Maltsev, LI Shekhtman, VK Vadakeppattu *Development of compact TPC for future Super Charm-Tau Factory detector* Nucl.Instrum.Meth.A, **1040**, C07021, 2022, https://doi.org/10.1016/j.nima.2022.167225
- V.K. Vadakeppattu and A.V. Sokolov 2024 JINST 19 P03007, *The result of simulation studies of a GEM-based TPC for the inner tracker of Super Charm-Tau Factory Detector at BINP* Journal of Instrumentation, **10.1088/1748-0221/19/03/P03007**

Acknowledgements

I would like to express my deepest gratitude to Dr. Andrey Sokolov, my supervisor, whose unwavering support, guidance, and expertise have been invaluable throughout my academic journey. His mentorship has been instrumental in shaping my research and professional development.

Special thanks to Prof. Dolgov, who played a pivotal role in my admission to the PhD program. I am grateful for the opportunity to pursue advanced studies under his mentorship.

I extend my sincere appreciation to the Russian Government for providing the scholarship that has made my academic pursuits possible. Their support has been crucial in facilitating my education and research endeavors.

I am thankful to Dr. LI Shekhtman for providing valuable technical guidance and insights. His expertise has been instrumental in navigating complex technical challenges and advancing my research.

I would also like to acknowledge the entire SCTF team for their support and collaboration. Their collective effort has enriched my academic experience and contributed to the success of my research endeavors.

Bibliography

1. *Conceptual design report* `https://ctd.inp.nsk.su/c-tau/`
2. *N. Brambilla et al. [Quarkonium Working Group], arXiv:hep-ph/0412158; N. Brambilla et al. [Quarkonium Working Group], arXiv:1010.5827; G.V. Pakhlova, P.N. Pakhlov and S.I.Eidelman, Phys. Usp. 53, 219 (2010).*
3. *C. Patrignani et al. (Particle Data Group), Chin. Phys. C 40, 100001 (2016)*
4. *W. J. Huo, T. F. Feng and C. x. Yue, Phys. Rev. D 67, 114001 (2003) [arXiv:hep-ph/0212211].*
5. *Y. Miyazaki et al. [Belle Collaboration], Phys. Lett. B 660, 154 (2008) [arXiv:0711.2189 [hep-ex]].*
6. *J. P. Ma, R. G. Ping and B. S. Zou, Phys. Lett. B 580, 163 (2004) [arXiv:hep-ph/0311012].*
7. *X. G. He, J. P. Ma and B. McKellar, Phys. Rev. D 47, 1744 (1993) [arXiv:hep-ph/9211276]*
8. *M. A. Sanchis-Lozano, Z. Phys. C 62, 271 (1994).*
9. *K. K. Sharma and R. C. Verma, Int. J. Mod. Phys. A 14, 937 (1999) [arXiv:hep-ph/9801202].*
10. *R. F. Lebed, R. E. Mitchell and E. S. Swanson, Prog. Part. Nucl. Phys. 93, 143 (2017)[arXiv:1610.04528 [hep-ph]].*
11. *S. Dubynskiy and M. B. Voloshin, Phys. Lett. B 666, 344 (2008) [arXiv:0803.2224 [hep-ph]].*
12. *C. J. Morningstar and M. J. Peardon, Phys. Rev. D 60, 034509 (1999) [arXiv:heplat/9901004].*
13. *S. Godfrey and N. Isgur, Phys. Rev. D 32, 189 (1985)*
14. *B. I. Eisenstein et al. [CLEO Collaboration], Phys. Rev. D 78, 052003 (2008) [arXiv:0806.2112 [hep-ex]]*
15. *M. Ablikim et al. [BESIII Collaboration], Phys. Rev. D 89 no.5, 051104 (2014) [arXiv:1312.0374 [hep-ex]].*
16. *A. Zupanc et al. [Belle Collaboration], JHEP 1309 139 (2013) [arXiv:1307.6240 [hep--ex]].*

17. *D. M. Asner and W. M. Sun, Phys. Rev. D 73, 034024 (2006) [arXiv:hep-ph/0507238].*
18. *S. Bianco, F. L. Fabbri, D. Benson and I. Bigi, Riv. Nuovo Cim. 26, 1 (2003) [arXiv:hepex/0309021].*
19. *A.Yu. Barnyakov, et al.PID System based on Focusing Aerogel RICH for the super c-τ factory,Nucl. Instrum. Methods Phys. Res.A (2019)*
20. *A.Yu. Barnyakov, et al., Nucl. Instrum. Methods A 732 (2013) 352–356*
21. *A.Yu. Barnyakov, et al., Nucl. Instrum. Methods A 766 (2014) 235.*
22. *A.Yu. Barnyakov, et al., Nucl. Instrum. Methods A 958 (2020)*
23. *S. Nishida, et al., Nucl. Instrum. Methods A 766 (2014) 28–31.*
24. *A.Yu. Barnyakov, et al., Nucl. Instrum. Methods A 639 (2011) 290–293*
25. *A.Yu. Barnyakov, et al., Nucl. Instrum. Methods A 553 (2005) 70–75*
26. *A.Yu. Barnyakov, et al., Nucl. Instrum. Methods Phys. Res. A 824 (2016) 79*
27. *I. Bedny et al., Nucl. Inst. Meth. A598 (2009) 273.*
28. *A. Boyarintsev, et al., JINST 11 (2016) P03013*
29. *V.L. Ivanov et al 2020 JINST 15 C07026*
30. *Ekaterina Prokhorova, Study of the fast calorimeter prototype for the Super Charm-Tau Factory, EPJ Web of Conferences 212, 01007 (2019)*
31. *D. R. Nygren. The time projection chamber: A new 4 pi detector for charged particles. PEP-0144.*
32. *D. R. Nygren, J. N. Marx, Physics Today 31 (1978) 46*
33. *Particle Detectors Claus Grupen. Teilchendetektoren. BI-Wissenschaftsverlag, 1993.* `https://doi.org/10.1017/CBO9780511534966`
34. *C. Ramsauer. Über den Wirkungsquerschnitt der Gasmoleküle gegenüber langsamen Elektronen. Annalen der Physik, 66:546, 1921.*
35. *W. P. Allis and P. M. Morse. Theorie der Streuung langsamer Elektronen an Atomen. Zeitschrift für Physik A, 70:567, 1931.*
36. *M. Gruwè. Gas studies for a TPC of a detector for the future Linear Collider TESLA, 1999.*
37. *W. Blum and L Rolandi. Particle Detection with Drift Chambers. Springer-Verlag,*

1993.

38. *F. Sauli. Gem: A new concept for electron amplification in gas detectors. Nucl.Instrum. Meth., A386:531–534, 1997* `http://dx.doi.org/10.1016/S0168-9002(96)01172-2`
39. `http://gdd.web.cern.ch/GDD/`
40. *F.Sauli, Nuclear Instruments and Methods in Physics A 805, (2016),2-24*
41. *Giomataris, Y.; Rebourgeard, Ph.; Robert, J.P.; Charpak, G. (1996) Nucl.Instrum. Meth.A 376 (1): 29–35.*
42. *TESLA technical design report, part IV "A Detector for TESLA", 2001. DESY 2001-011, ECFA 2001-209.*
43. `https://gaudi.web.cern.ch/gaudi/`
44. `https://indico.cern.ch/event/275698/attachments/499658/690245/DD4hep.pdf`
45. `https://geant4.web.cern.ch/`
46. *GENFIT – a Generic Track-Fitting Toolkit* `https://indico.cern.ch/event/258092/papers/1588579/files/4253-genfit.pdf`
47. *Simulation of different options of the Inner Tracker for Novosibirsk Super Charm-Tau Factory Detector T.V. Maltsev, L.I. Shekhtman, A.V. Sokolov and V.K. Vadakeppattu* `https://doi.org/10.1051/epjconf/201921201011`
48. *The design, construction, operation and performance of the Belle II silicon vertex detector Belle-II SVD Collaboration•K. Adamczyk* `https://doi.org/10.1088/1748-0221/17/11/P11042`
49. *The ALICE silicon strip detector system, P Kuijer, for the Alice collaboration* `https://doi.org/10.1016/S0168-9002(00)00196-0`
50. *The micro-Resistive WELL detector: a compact spark-protected single amplification-stage MPGD, G. Bencivenni, R. De Oliveira, G. Morello and M. Poli Lener* `10.1088/1748-0221/10/02/P02008`
51. *L. Shekhtman, et al., Nucl. Instrum. Methods A 936 (2019) 401-404*
52. *The -RWELL for high rate application, G. Bencivenni et al 2020 JINST 15 C09034* `10.1088/1748-0221/15/09/C09034`

53. *V.K. Vadakeppattu et al 2020 JINST 15 C07021* `10.1088/1748-0221/15/07/C07021`

54. `https://garfieldpp.web.cern.ch/garfieldpp/`

55. `https://magboltz.web.cern.ch/magboltz/`

56. *V.K. Vadakeppattu and A.V. Sokolov 2024 JINST 19 P03007* `10.1088/1748-0221/19/03/P03007`

57. `https://www.comsol.com/`

58. *C. Geuzaine and J.-F. Remacle, "Gmsh: a three-dimensional finite element mesh generator with built-in pre-and post-processing facilities," International Journal for Numerical Methods in Engineering, vol. 79, pp. 1309–1331, 2009.*

59. *C. I. C. for Science, Elmer: Open Source Finite Element Software for Multiphysical Problems,* `http://www.csc.fi/english/pages/elmer`.

60. *ALICE collaboration, Upgrade of the ALICE Time Projection Chamber, Tech. Rep.,CERN-LHCC-2013-020 [ALICE-TDR-016] (2013).*

61. *L. Shekhtman, F. Ignatov and V. Tayursky, Simulation of physics background in Super c-tau factory detector, EPJ Web Conf. 212 (2019) 01009.*

62. *J. Adolfsson, ALICE TPC Collaboration, The upgrade of the ALICE TPC with GEMs and continuous readout, JINST 16 (2021) P03022*

List of Figures

List of Tables